

# 1     **A quantitative biophysical principle to explain the 3D cellular** 2                                   **connectivity in curved epithelia**

3  
4  
5  
6  
7  
8

*Pedro Gómez-Gálvez<sup>1,2,3,4\*,†</sup>, Pablo Vicente-Munuera<sup>1,2,5†</sup>, Samira Anbari<sup>6,7†</sup>, Antonio Tagua<sup>1,2,†</sup>, Carmen Gordillo-Vázquez<sup>1,2</sup>, Jesús A. Andrés-San Román<sup>1,2</sup>, Daniel Franco-Barranco<sup>8,9</sup>, Ana M. Palacios<sup>1,2</sup>, Antonio Velasco<sup>1</sup>, Carlos Capitán-Agudo<sup>1</sup>, Clara Grima<sup>10</sup>, Valentina Annese<sup>1,2</sup>, Ignacio Arganda-Carreras<sup>8,9,11</sup>, Rafael Robles<sup>10</sup>, Alberto Márquez<sup>10</sup>, Javier Buceta<sup>12,\*</sup>, Luis M. Escudero<sup>1,2,\*</sup>*

9     <sup>1</sup>*Instituto de Biomedicina de Sevilla (IBiS), Hospital Universitario Virgen del Rocío/CSIC/Universidad de*  
10     *Sevilla and Departamento de Biología Celular, Universidad de Sevilla. 41013 Seville, Spain*

11     <sup>2</sup>*Biomedical Network Research Centre on Neurodegenerative Diseases (CIBERNED), Madrid, Spain*

12             <sup>3</sup>*Current address: MRC Laboratory of Molecular Biology, Cambridge, UK*

13             <sup>4</sup>*Current address: Department of Physiology, Development and Neuroscience, University of*  
14             *Cambridge, UK*

15             <sup>5</sup>*Current address: Laboratory for Molecular Cell Biology, University College London. London, UK*

16             <sup>6</sup>*Chemical and Biomolecular Engineering Department, Lehigh University.*

17                                   *Bethlehem, PA 18018, USA*

18             <sup>7</sup>*Current address: Biomedical Engineering Department, Johns Hopkins University. Baltimore, MD*  
19             *21205, USA*

20             <sup>8</sup>*Department of Computer Science and Artificial Intelligence, University of the Basque Country*  
21             *(UPV/EHU). San Sebastian, Spain*

22                                   <sup>9</sup>*Donostia International Physics Center (DIPC). San Sebastian, Spain*

23             <sup>10</sup>*Departamento de Matemática Aplicada I, Universidad de Sevilla. Seville 41012, Spain*

24                                   <sup>11</sup>*Ikerbasque, Basque Foundation for Science. Bilbao, Spain*

25             <sup>12</sup>*Institute for Integrative Systems Biology (I<sup>2</sup>SysBio), CSIC-UV, Paterna (Valencia) 46980, Spain*

26  
27

28     <sup>†</sup>These authors contributed equally to this work.

29     <sup>\*</sup>Corresponding authors

## 1 SUMMARY

2 Epithelial cell organization and the mechanical stability of tissues are closely related.  
3 In this context, it has been recently shown that packing optimization in  
4 bended/folded epithelia is achieved by a surface tension energy minimization  
5 mechanism that leads to a novel cellular shape: the *scutoid*. However, further cellular  
6 and tissue level implications of this new developmental paradigm remain unknown.  
7 Here we focus on the relationship between this complex cellular shape and the  
8 connectivity between cells. We address this problem using a combination of  
9 computational, experimental, and biophysical approaches in tubular epithelia. In  
10 particular, we examine how energy drivers affect the three-dimensional packing of  
11 these tissues. We challenge our biophysical model by reducing the cell adhesion in  
12 epithelial cells. As a result, we observed an increment on the cell apico-basal  
13 intercalation propensity that correlated with a decrease of the energy barrier  
14 necessary to connect with new cells. We conclude that tubular epithelia satisfy a  
15 quantitative biophysical principle, that links tissue geometry and energetics with the  
16 average cellular connectivity.

17

18

## 19 KEYWORDS

20 Tissue/Cellular Biophysics, Computational geometry, Developmental Systems  
21 Biology, Mathematical/Biophysical modeling, Bioimage Analysis

22

## 1 INTRODUCTION

2 During the last decades much progress has been achieved in the understanding of  
3 the emergence of self-organization in tissues. This problem has been addressed from  
4 the viewpoint of energetics considerations (Alt et al., 2017; Canela-Xandri et al.,  
5 2011; Fletcher et al., 2014; Misra et al., 2017; Nelson et al., 2005; Siedlik et al., 2017;  
6 Sugimura et al., 2016; Trepatt et al., 2009), material-like properties (Bi et al., 2015;  
7 Campàs et al., 2014; Latorre et al., 2018; Mongera et al., 2018; Pérez-González et al.,  
8 2019; Yang et al., 2017), and the analysis of the cellular packing (Curran et al., 2017;  
9 Farhadifar et al., 2007; Gibson et al., 2006; Gibson et al., 2011; Gómez et al., 2021;  
10 Honda, 1978; Lewis, 1928; Mao et al., 2013; Sanchez-Gutierrez et al., 2016;  
11 Thompson, 1945). As for the latter, the analysis of epithelial surfaces as tessellations  
12 of convex polygons has revealed mathematical and physical principles with biological  
13 consequences. One well-known example are the implications of the celebrated  
14 Euler's formula,  $V - E + F = \chi$  (**STAR Methods**) (Euler, 1767). This formula implies  
15 that cells in packed tissues have, on average, six neighbors (i.e., the average cellular  
16 connectivity on a surface reads  $\langle n_{2D} \rangle = 6$ ) (Reinhardt, 1918; Wetzel, 1926). This  
17 principle has biological consequences, for example, the degree of cellular  
18 connectivity regulates the strength of the cell-cell juxtacrine signaling (Guignard et  
19 al., 2020; Sharma et al., 2019; Tung et al., 2012).

20 For a long time, the validity of this mathematical concept (i.e., each cell, on average,  
21 connects with six neighboring cells) has been assumed in three dimensions (3D):  
22  $\langle n_{2D} \rangle = 6 \implies \langle n_{3D} \rangle = 6$ . Such an assumption is rooted in the common idealization  
23 of epithelial cells as regular prismatic solids in either planar or bended epithelia.  
24 However, the recent discovery of more complex cellular shapes in epithelia, i.e.,  
25 scutoids, that achieve an efficient 3D tissue packing has set a new paradigm that has  
26 not been yet fully explored (**Box A**) (Gómez-Gálvez et al., 2018; Mughal et al., 2018;  
27 Rupprecht et al., 2017). Scutoidal cellular shapes are the result of intercalations  
28 among cells along the apico-basal axis (**Box A-C** and **Fig. 1A**). This phenomenon is  
29 then a spatial version of the so-called T1 transitions that produce rearrangements of  
30 neighboring cells in the plane as a function of time in numerous developmental  
31 processes (**Box B**) (Bertet et al., 2004; Irvine and Wieschaus, 1994; Spencer et al.,

1 2017). Importantly, scutoids imply necessarily changes in the neighboring  
2 relationship between cells in a 3D spatial context and, consequently, modify the  
3 connectivity properties of cells (**Box C**). Still, the analysis of tissue organization in 3D  
4 and the corresponding biophysical insight have been hindered by the technical  
5 difficulties to accurately segment and 3D-reconstruct cells, especially in curved  
6 tissues. In addition, very few computational models account for the presence of  
7 apico-basal transitions to investigate 3D self-organization in tissues (Gómez-Gálvez et  
8 al., 2018; Ioannou et al., 2020; Mughal et al., 2018; Okuda et al., 2019; Rupprecht et  
9 al., 2017). Moreover, from an energetics viewpoint, while the appearance of scutoids  
10 can be explained by a minimal model based on a surface/line tension minimization  
11 mechanism (Gómez-Gálvez et al., 2018; Mughal et al., 2018; Okuda et al., 2019;  
12 Rupprecht et al., 2017), the role played by additional energetic contributions to  
13 modulate the frequency of apico-basal intercalations is unknown.

14 The analysis of 3D packing is in turn utterly relevant in cubic and columnar  
15 monolayer tubular epithelia, where scutoids appear more frequently (Gómez-Gálvez  
16 et al., 2018; Gómez et al., 2021; Iruela-Arispe and Beitel, 2013; Sanchez-Corrales et  
17 al., 2018). Epithelial tubes are in fact the primary developmental structures in all  
18 organisms with bilateral symmetry (Gilbert and Barresi, 2013), and tubulogenesis is  
19 fundamental in a broad variety of key developmental processes, including  
20 gastrulation and neurulation (Colas and Schoenwolf, 2001; Iruela-Arispe and Beitel,  
21 2013; Leptin and Grunewald, 1990; Nelson, 2009; Pilot and Lecuit, 2005; Röper, 2018;  
22 Swanson and Beitel, 2006). Furthermore, epithelial tubes are the essential functional  
23 unit of many mammalian organs, including glands, components of the digestive  
24 apparatus, lungs, and kidney (Huebner and Ewald, 2014).

25 Here, we study the packing and the 3D cellular connectivity properties of epithelial  
26 tubes. We analyze the effect of different energetic contributions to modulate the  
27 frequency of apico-basal intercalations; demonstrate that the presence of scutoids  
28 implies a breakdown of the principle  $\langle n_{3D} \rangle = 6$ ; and reveal a quantitative biophysical  
29 principle that links the 3D cellular connectivity, energetics, and geometrical  
30 descriptors (e.g., tissue curvature/thickness). Our findings are supported by i) a  
31 computational model that realistically renders the 3D cellular organization of tubular

1 epithelia (including the appearance of scutoids); ii) experimental data of wildtype  
2 (wt) and mutant epithelial tubes (*Drosophila's* salivary gland) whose 3D cellular  
3 structure has been accurately characterized by means of a computer-aided image  
4 analysis pipeline. And iii), a biophysical model, supported by mathematical  
5 calculations, that connects the tissue energetics with the 3D organization of epithelial  
6 tubes.

7

## 8 RESULTS

### 9 The Voronoi computational tubular model supports a relationship between energy 10 profiles and the intercalation propensity

11 To understand how the geometry of tubular epithelia and different energy  
12 contributions affect the 3D cellular packing and connectivity of these tissues, we  
13 designed and implemented a computational epithelial model that follows the  
14 principles of Voronoi tessellations (**Box D, E**) (Gómez-Gálvez et al., 2018). In brief, we  
15 generated 3D models of epithelial tubes by populating with seeds the apical surface,  
16  $\Sigma_a$  (light blue points in **Fig. 1B**) and implementing normal projections of those seeds  
17 up to the basal surface,  $\Sigma_b$  (dark blue points in **Fig. 1B**). Each seed and its projection  
18 corresponded to an individual cell of a tube. At each surface section  $\Sigma$  (from apical to  
19 basal) a 2D Voronoi diagram was performed, and the collection of those tessellations  
20 rendered the 3D cellular geometry of cells (see details in **STAR Methods**). We point  
21 out that we do not implement any temporal dynamics to the seeds. Thus, our  
22 computational model is suited to static epithelial configurations as the ones  
23 experimentally reported herein (see below).

24 Epithelial tubes appear in nature with very different thicknesses and cellular  
25 arrangements. In order to explore how these features influence the 3D packing  
26 properties of tubular epithelia we built diverse *in silico* Voronoi tubes. First, to  
27 investigate the effect of tissue thickness we computed Voronoi tubes with different  
28 surface ratios  $s = R/R_a$  ( $R$  and  $R_a$  being the radial coordinate of the tube and the  
29 apical radius respectively, **Fig. 1C, D**). We used  $s$ -steps of 0.5 up to  $s = 10$ , so we  
30 were able to explore 19 different values of the basal radius,  $R_b$  (**Fig. 1D**). Second, we  
31 generated 10 different configurations in terms of the disorder level of the spatial

1 positions of the cellular seeds on the apical surface and the corresponding Voronoi  
2 tessellations (V1 to V10, **Fig. 1D**). To that end, we used a fully random Voronoi  
3 tessellation, i.e., randomized positions of cellular seeds, as the most disordered  
4 pattern (V1). That configuration was made progressively more uniform (i.e., spatially  
5 ordered) after nine successive iterations of the homogenizing Lloyd's algorithm (**Box**  
6 **E** and **STAR Methods**) (**Fig. 1D**). The resulting set of 10 different cellular  
7 arrangements (V1 to V10) with increasing order properties conforms a Centroidal  
8 Voronoi Tessellation (CVT) scale that has been proved useful to analyze the effect of  
9 the topological organization of tissues and to simulate different tissues and/or  
10 pathological conditions (Sanchez-Gutierrez et al., 2016; Vicente-Munuera et al.,  
11 2020). We used the CVT scale to investigate how the average number of apico-basal  
12 intercalations per cell,  $\langle i \rangle$ , changes as a function of the apico-basal coordinate,  $s$ , and  
13 the disorder level (**Fig. 1D**). As previously reported, we found that the number of  
14 apico-basal transitions (**Fig. 1D**) and scutoids (**Fig. S1**) increased with  $s$  (Gómez-  
15 Gálvez et al., 2018). As for the effect of the disorder level, we found that only in the  
16 case of fully disordered tubes (i.e., V1: random case), and for low values of  $s$ , there  
17 are more intercalations, whereas for the rest of cases we observed that  $\langle i \rangle$  is fairly  
18 independent of the CVT scale (**Fig. 1D**).

19 Energy contributions can be linked to geometric features of the shapes of epithelial  
20 cells (Alt et al., 2017), see **Box F-H**. We used the set of Voronoi tubes (V1 to V10) to  
21 explore surface tension, elasticity, and apical contractility energies, since these  
22 energy contributions have been shown to play key roles in the organization of  
23 epithelia (Alt et al., 2017; Farhadifar et al., 2007). As a first step, we estimated the  
24 average cellular energy profiles as a function of  $s$  in the computational tubular model  
25 (**Fig. 1E-G**). The average surface tension energy (**Box F**) is related to the average  
26 lateral area of the cells,  $\langle A \rangle$ , and therefore increase with the surface ratio,  $s$ . Our  
27 results revealed that  $\langle A \rangle$  is seemingly independent of the CVT scale (**Fig. 1E**).  
28 Consequently, the average cell surface tension energy profile does not depend on the  
29 level of the topological disorder. The contractile energy (**Box G**) is related to the  
30 average and the variance of the apical perimeter,  $L$ , (Gilbert and Barresi, 2013;  
31 Farhadifar et al., 2007) therefore it does not depend on the surface ratio,  $s$ . The

1 Voronoi model revealed that  $\langle L \rangle$  is CVT independent, but the apical perimeter  
2 fluctuations decrease as the CVT scale increases (**Fig. 1F**). Finally, the average cell  
3 elastic energy (Gelbart et al., 2012; Odell et al., 1981) depends on the average and  
4 the variance of the cellular volume (**Box H**). Since the average cell volume  $\langle V \rangle$  is, by  
5 construction, independent of the CVT scale (**STAR Methods**), the average cellular  
6 elastic energy increases with the cellular volume fluctuations, that in turn decrease  
7 with the CVT scale (**Fig. 1G**).

8 In order to evaluate how the appearance of scutoids is modulated by these energy  
9 contributions for different values of the tissue thickness, we computed the cross-  
10 correlation functions,  $C(s)$ , between the average cellular energy profiles,  $\langle E_Z \rangle$  ( $Z$   
11 being  $A$  or  $V$ , i.e., surface tension or elastic terms), and the average number of apico-  
12 basal intercalations,  $\langle i \rangle$  (**Fig. 1H** and **STAR Methods**). The cross-correlation measures  
13 the similarity between two signals as a function of the displacement (or lag) of one  
14 signal relative to the other. In our case the displacement/lag refers to the apico-basal  
15 coordinate,  $s$ , and consequently we inquire into the possibility that energetic  
16 contributions either precede or follow the appearance of apico-basal intercalations.  
17 Our results indicate that maximum correlations are obtained at zero lag  
18 independently of the disorder level and that the appearance of scutoids correlates  
19 more significantly with the surface tension energy profile than with the elastic  
20 energy: 95% vs. 80% respectively. The latter is in agreement with previous studies  
21 that have shown that surface tension energy minimization is the main cause  
22 underlying the appearance of scutoids (Gómez-Gálvez et al., 2018; Gómez et al.,  
23 2021; Mughal et al., 2018). Also, when assessing the extra effect of the energy input  
24 due to the apical contractility term to the surface tension energy,  $\langle E_A \rangle + \langle E_L \rangle$ , we  
25 found that it increases the correlation between energy profile and the number of  
26 intercalations up to 98%, but it does not lead to any change in the correlation due to  
27 elastic terms,  $\langle E_V \rangle + \langle E_L \rangle$  (**Fig. 1H**).

28 We further examined the cross-correlation between the gradient of cellular  
29 intercalations along the apico-basal axis,  $\partial_s \langle i \rangle = \partial \langle i \rangle / \partial s$ , and the gradient of the  
30 energy,  $\partial_s \langle E_Z \rangle$ . In this way, we evaluated the level of correspondence between the  
31 variation of the number of intercalations and the changes of the energy as a function

1 of the radial coordinate,  $s$ . We found that, independently of the CVT scale,  $\partial_s \langle i \rangle$   
2 correlates slightly stronger with changes in the surface tension energy,  $\partial_s \langle E_A \rangle$ , than  
3 with changes of the elastic contribution,  $\partial_s \langle E_V \rangle$ :  $\sim 80\%$  versus  $\sim 75\%$  respectively at  
4 optimal lag (**Fig. 1I**). Interestingly,  $\partial_s \langle i \rangle$  lags behind  $\partial_s \langle E_Z \rangle$ , i.e., the optimal lag for  
5 which  $C(s)$  is the largest is located at  $s > 0$ . Therefore, energy variations along the  
6 apico-basal axis seem to precede changes in the number of intercalations that, in  
7 turn, suggests an instructive role of the former over the latter.

8 Summing up, the Voronoi tubular model supports the idea that surface tension  
9 energy is the more relevant contribution regulating the appearance of apico-basal  
10 intercalations, and suggests that elastic terms play a role, yet less important than  
11 surface tension, for modulating the intercalation propensity (see **Discussion**).

12

### 13 **The Voronoi tubular model suggests a link between 3D tissue packing and energy** 14 **cues**

15 To link quantitatively energy traits and 3D packing, we implemented a benchmark  
16 able to simultaneously reveal the existence of apico-basal intercalations (scutoids)  
17 and the polygonal distribution of cells at the apical and the basal surfaces. To that  
18 end, we computed the probability that cells change their polygonal class between the  
19 apical and basal surfaces. Thus, the components (i.e., bins) of this distribution along  
20 the diagonal account for cells that have the same polygonal class at apical and basal  
21 surfaces, whereas the spreading away from the diagonal ensures the existence of  
22 scutoids and, consequently, changes in the cellular 3D connectivity (**Fig. 2A** and **STAR**  
23 **Methods**). Our data revealed that, regardless of the value of the tissue thickness (and  
24 the CVT scale), the dominant apical-basal polygonal class corresponds to cells with six  
25 neighbors (**Fig. 2A**). As the tissue thickness,  $s_b = R_b/R_a$ , increases, more scutoidal  
26 shapes with a distinct number of neighbors in apical and basal surfaces appeared.  
27 This feature was revealed by the increasing value of the spreading away from the  
28 diagonal,  $\eta^2$  (**STAR Methods** and **Table S1**). In that regard, in agreement with the  
29 results shown in **Fig. 1D-G**, our data indicates that  $\eta^2$  increases with the tissue  
30 thickness and decreases with the CVT scale (**Fig. 2B**). Also, the cross-correlation  
31 analysis between the spreading coefficient and energy profiles agrees with **Fig. 1H**

1 and reveals that independently of the CVT scale the neighbor exchanges correlate  
2 more strongly with the surface tension energy profile than with the elastic  
3 contribution: 90% vs. 70% at zero (optimal) lag (**Fig. 2C**). Furthermore, we computed  
4 the average number of total contacts between cells (i.e., the average 3D cellular  
5 connectivity),  $\langle n_{3D} \rangle$ , as a function of the surface ratio (i.e., the radial coordinate) and  
6 the Voronoi class (i.e., the level of cellular disorder in the tissue) (**Fig. S1**). Our data  
7 indicated, that cells, on average, are connected to more than six cells, i.e.,  $\langle n_{3D} \rangle > 6$ ,  
8 and the results are quantitatively consistent with a mathematical derivation that  
9 shows that  $\langle n_{3D} \rangle$  is linearly proportional to the number of apico-basal intercalations  
10  $\langle i \rangle$ :  $\langle n_{3D} \rangle = 6 + \langle i \rangle / 2$  (**STAR Methods** and **Fig. S1**).

11

## 12 **The Voronoi tubular model recapitulates the properties of *in vivo* epithelial tubes**

13 In order to compare the results obtained in our Voronoi computational tubular  
14 models against the properties found in real tissues, we implemented a  
15 methodological pipeline that combines several image analysis techniques to  
16 accurately reconstruct the 3D shapes of cells of *in vivo* epithelial tubes (Arganda-  
17 Carreras et al., 2017; Franco-Barranco et al., 2021; Machado et al., 2019) (**STAR**  
18 **Methods**). We used the *Drosophila* larval salivary gland, a cubic monolayer  
19 epithelium, as a model due to its ideal characteristics to study complex tubular  
20 developmental structures (Girdler and Roper, 2014) (**Fig. 3A**). Also, cellular growth  
21 and division, as well as possible global tissue deformation processes, do not occur in  
22 the *Drosophila*'s salivary gland at the developmental stage of our observations (i.e.  
23 the tissue is static); a fact that enables the comparison with the Voronoi  
24 computational model.

25 We determined the average basal surface ratio (thickness) of the salivary glands,  
26  $\langle s_b \rangle = 8.5 \pm 1.1$ , the average percentage of scutoids,  $72 \pm 12\%$ , the average 3D  
27 connectivity,  $\langle n_{3D}(s_b) \rangle = 6.6 \pm 0.2$ , and the average number of apico-basal  
28 intercalations per cell,  $\langle i(s_b) \rangle = 1.2 \pm 0.3$ , thus confirming *in vivo* the validity of the  
29 formula  $\langle n_{3D} \rangle = 6 + \langle i \rangle / 2$  (**STAR Methods** and **Fig. S1**). We also calculated the  
30 spreading coefficient of the 3D connectivity,  $\eta^2 = 1.2 \cdot 10^{-2}$ , (**Fig. 3B**), and the 2D  
31 polygonal distributions in the apical and basal surfaces (**Fig. S2**). Interestingly, we

1 observed a small, but significant, increase of the number of hexagons on the basal  
2 surface of the wt glands (see **Fig. S2, Table S1**).

3 Further, in order to derive how energy contributions change as a function of the  
4 apico-basal coordinate,  $s$ , we implemented an algorithm that obtains the concentric  
5 radial sections of *in vivo* tubes from apical to basal (Yang et al., 2019) (**STAR**  
6 **Methods**). These sections were used to quantify as a function of the surface ratio,  $s$ ,  
7 the number of apico-basal intercalations,  $\langle i(s) \rangle$ , the average lateral area,  $\langle A(s) \rangle$ , and  
8 the cellular volume fluctuations,  $\sigma_V^2(s)$  (**Fig. 3C**). Similarly to the procedure that we  
9 implemented in the Voronoi tubular model (**Fig. 1H, I**), we used these *in vivo* data to  
10 perform a cross-correlation analysis between  $\langle i \rangle$  and the energy contributions  $\langle E_Z \rangle$   
11 ( $Z$  being  $A$  or  $V$ , i.e., surface tension or elastic terms). The results indicated that *in*  
12 *vivo* intercalations also correlate stronger with surface tension energy contributions  
13 than with elastic terms:  $\sim 98\%$  vs.  $\sim 90\%$  at zero (optimal) lag (**Fig. 3D**). We also found  
14 that in this case, by including the extra contribution from the apical contractile  
15 energy to the surface tension energy, i.e.  $\langle E_A \rangle + \langle E_L \rangle$ , slightly decreases the  
16 correlation down to  $\sim 95\%$  (optimal lag) but does not modify that of the elastic term,  
17 i.e.  $\langle E_V \rangle + \langle E_L \rangle$  (**Fig. 3D**). As for the cross-correlation between  $\partial_s \langle i \rangle$  and  $\partial_s \langle E_Z \rangle$ , we  
18 also found that in *in vivo* tubes it is more significant for the case of the surface  
19 tension energy,  $\sim 80\%$ , than for the elastic contribution,  $\sim 70\%$ . In addition, we also  
20 observed a positive lag for  $\partial_s \langle E_V \rangle$  that suggests an instructive role of elastic energy  
21 variations towards changes in the number of apico-basal intercalations (**Fig. 3E**).

22 Subsequently, we sampled the Voronoi tubular model in terms of the disorder  
23 configuration (CVT scale) and the value of the thickness,  $s_b$ , that leads to a tube that  
24 represents the aforementioned properties observed *in vivo*. We found that the V8 *in*  
25 *silico* model with  $s_b = 1.75$  displayed a scutoidal prevalence,  $79 \pm 5\%$ , average  
26 number of 3D neighbors,  $6.72 \pm 0.08$ , average number of apico-basal intercalations  
27 per cell,  $1.4 \pm 0.1$ , and value of the 3D histogram spreading,  $\eta^2 = 1.4 \cdot 10^{-2}$ ,  
28 comparable to those found in *in vivo* tubes (**Fig. S3**). Further, the 2D polygonal  
29 distributions in the apical and basal surfaces of the V8 model ( $s_b = 1.75$ ) were found  
30 to be similar and in agreement with those found in wt salivary glands (**Fig. S2** and  
31 **Table S1**). We also observed that the increment apico-basal transitions by means of a

1 larger surface ratio ( $s_b = 10$ ) leads to an increase of topological disorder (larger  
2 variance of cell sidedness, see **Fig. S2** and **Table S1**); a phenomenon that is similar to  
3 that observed in T1-transitions (Blankenship et al., 2006; Zallen and Zallen, 2004).  
4 Finally, we implemented the cross-correlation analyses between intercalations and  
5 energy contributions in the V8 model ( $s_b = 1.75$ ). We obtained similar features as  
6 those obtained *in vivo*, including the suggested instructive role of elastic energy  
7 variations towards changes in the number of apico-basal intercalations (**Fig. S3**).  
8 Altogether, we concluded that the V8 model ( $s_b = 1.75$ ) reproduces the 2D and 3D  
9 packing properties of the *Drosophila*'s larval salivary glands.

10

## 11 **A biophysical model explains the cellular connectivity observed in *in silico* and in** 12 ***in vivo* tubular epithelia**

13 In order to explain how the number of 3D neighbors of a cell (i.e., the cellular  
14 connectivity) changes as a function of the apico-basal coordinate, we developed a  
15 biophysical model. The model is based on a Kolmogorov rate equation and accounts  
16 for the probability of cells to increase their 3D connectivity as the radial coordinate  
17 along the apico-basal axis changes from  $s$  to  $s + ds$  (**Fig. 4A, B** and **STAR Methods**):

$$18 \quad \frac{dP_m(s)}{ds} = P_{m-1}(s)r_{m-1,m} - P_m(s)r_{m,m+1} \quad (1)$$

19 This equation determines, as a function of  $s$ , the set of probabilities  $\{P_m(s)\} =$   
20  $P_3(s), P_4(s), \dots, P_{N_{max}}(s)$ , i.e., the fractions of cells with a given number,  $m$ , of 3D  
21 neighbors such that  $\sum_m P_m(s) = 1$ . Thus, the average 3D cellular connectivity (i.e.,  
22 the average number of 3D neighbors per cell) as a function of  $s$  reads  $\langle n_{3D}(s) \rangle =$   
23  $\langle m \rangle = \sum_m m P_m(s)$ .

24 In Eq. (1),  $r_{m,m+1}$  accounts for the transition “rate” at which 3D are gained, i.e., the  
25 probability per unit of  $s$  to increase the cellular connectivity by one cell. By drawing  
26 parallels between apico-basal intercalations and planar T1 transitions (Bi et al., 2014;  
27 Gómez-Gálvez et al., 2018; Sanchez-Corrales et al., 2018) we assumed, following the  
28 Eyring model (Eyring, 1935), that cells need to overcome an energy barrier,  $\Delta E_m(s)$ ,  
29 to gain a new 3D neighbor, that is,  $r_{m,m+1} \sim e^{-\Delta E_m(s)}$  (**Fig. 4A, B**). Our experimental,  
30 computational, and analytical results (see **STAR Methods** and **Figs. S4, S5**) support

1 the idea that  $r_{m,m+1} = \alpha(N_{max} - m)e^{-m\beta(s)}$ , where  $\alpha$  is a ‘bare’ transition “rate”,  
2  $\beta(s)$  accounts for the energy cost required to gain one 3D neighbor at a given  
3 position of the apico-basal coordinate,  $s$ , and  $N_{max}$  is the maximum possible 3D  
4 cellular connectivity for a cell (i.e., if  $m = N_{max}$  then  $r_{m,m+1} = 0$ ) (**STAR Methods**).  
5 This model predicts a logistic-like growth of the cellular connectivity (**STAR Methods**).  
6 In order to assess the validity of our model we implemented a fitting/optimization  
7 procedure that provides the value of the model parameters that minimize the error  
8 in the fitting of the curve  $\langle n_{3D}(s) \rangle$  (**STAR Methods**). Our results show an excellent  
9 agreement for all values of the CVT scale (**Fig. S6, Table S1**), the computational  
10 tubular model that represents the best in vivo data, i.e. V8 ( $s_b = 1.75$ ) (**Fig. 4C**), and  
11 the wt salivary glands (**Fig. 4D**). We further assessed the goodness of the biophysical  
12 model by predicting accurately the 3D neighbor’s distribution as a function of the  
13 apico-basal coordinate,  $\{P_m(s)\}$  (**Fig. 4C, D, Fig. S6**).

14

## 15 **Genetic perturbations modify the 3D cellular connectivity properties of epithelial** 16 **tubes**

17 Our analyses suggest that surface tension is the energy contribution that affects the  
18 propensity of apico-basal intercalations the most. Surface tension energy originates  
19 in adhesion-mediated interactions between cells that ultimately modulate the  
20 magnitude of cell-cell contacts. Following these ideas, we explored the role of cell-  
21 cell adhesion by experimentally reducing the amount of the E-cadherin (E-cadh). For  
22 this aim, we overexpressed a *UAS-RNAi* line specific for the *shotgun* (*shg*) gene on the  
23 developing *Drosophila* salivary gland (Brand and Perrimon, 1993; Hammond et al.,  
24 2000; Tepass et al., 1996) (**STAR Methods**). We compared the E-cadh antibody  
25 fluorescence profiles in wt and the mutant glands ( $\Delta Ecad$ ) and confirmed the  
26 reduction of E-cadh levels in the latter (**Fig. S7**). The cells in the  $\Delta Ecad$  glands bulged  
27 at the basal surface and were smaller than the wt cells (**Fig. 5A, Table S1, Fig. S7**). We  
28 processed these glands to extract their 3D cellular connectivity features and average  
29 energy profiles (**STAR Methods** and **Table S1**). We determined the effective average  
30 basal surface ratio (**STAR Methods**) of the mutant salivary glands  $\langle s_b \rangle = 7.4 \pm 0.8$ ,  
31 the average percentage of scutoids,  $65 \pm 14\%$ , the average 3D connectivity,

1  $6.5 \pm 0.2$ , and the average number of apico-basal intercalations per cell,  $1.1 \pm 0.4$ ,  
2 (Table S1 , Fig. S7). These values confirm the validity of the formula  $\langle n_{3D} \rangle = 6 +$   
3  $\langle i \rangle / 2$  in this genetic background too. Also, the cross-correlation analysis revealed  
4 that the surface tension energy remained as the main energy contribution (Fig. S8).  
5 Thus,  $\Delta E_{cad}$  and wt glands reached the same 3D connectivity although the effective  
6 surface ratio of the former was smaller (Table S1). These results suggest that a  
7 decrease in the cellular adhesion facilitates the emergence of apico-basal  
8 intercalations.

9

### 10 **The reduction of cellular adhesion decreases the activation energy required to** 11 **produce apico-basal intercalations**

12 The fitting/optimization procedure of the mutant data showed, as in the case of the  
13 wt phenotype and the *in silico* tubes, an excellent agreement (Fig. 5B) that allowed  
14 us to estimate the energy-related parameters as summarized by  $\alpha$  and  $\beta(s)$  (Fig. 5C  
15 and Table S1). The estimation of  $\alpha$  and  $\beta(s)$  in wt and mutant tubes indicated that  
16 the energy required to gain an additional neighbor,  $\beta(s)$ , is larger in *in vivo* tubes  
17 than in the computational model independently of the CVT scale (Fig. 5C, Fig. S9,  
18 Table S1), see Discussion. Finally, the results obtained from the analysis of the  
19 mutant glands confirmed that a decrease in the cellular adhesion facilitates the  
20 emergence of apico-basal intercalations since the activation energy gets reduced in  
21 the  $\Delta E_{cad}$  phenotype when compared to the wt case (Fig. 5B and 5C, and Table S1).  
22 In particular, in the mutant case, the curve that describes the energetic cost to gain  
23 new neighbors as a function of the apico-basal coordinate,  $\beta(s)$ , lies below the curve  
24 of the wt background (Fig. 5C) and we found that the average energy cost,  $\bar{\beta}$  (STAR  
25 Methods), is  $\sim 43\%$  larger in the wt case:  $\bar{\beta}_{\Delta E_{cad}} = 0.46$  and  $\bar{\beta}_{wt} = 0.65$ . Altogether,  
26 when we challenged the biophysical model with the perturbation experiment, we  
27 obtained the expected results: smaller cellular adhesion leads to a smaller energetic  
28 cost to gain new neighbors.

29

### 30 **DISCUSSION**

1 Here we have shown how a biophysical principle underlies the emergence of  
2 functionally complex 3D developmental structures. Namely, cells increase their 3D  
3 connectivity in a logistic-like fashion by means of apico-basal intercalations that  
4 require overcoming an energy barrier that grows with the number of 3D neighbors.  
5 Thus, our analyses explain how the presence of the novel paradigm of epithelial cells'  
6 shape and packing, the *scutoid*, affects the cellular connectivity in the third  
7 dimension. In that regard, we have shown how the 3D cellular connectivity and  
8 tissue energetics are coupled, and we have proposed a quantitative biophysical  
9 model to explain that relationship.

10 Our biophysical model relies on a phenomenon observed in the Voronoi  
11 computational simulations, supported by mathematical arguments, and confirmed in  
12 experiments: the “poor get richer” principle (see **STAR Methods**). Roughly speaking,  
13 we have shown that the fewer neighbors a cell has on a surface, the larger is the  
14 probability of a 3D cellular connectivity increase. Interestingly, a similar idea has been  
15 reported in T1 dynamical processes during the remodeling of planar epithelia where  
16 it has been shown that the energy barrier associated with cellular remodeling, rather  
17 than being constant, depends on the cellular environment (Bi et al., 2014). Since the  
18 scutoidal geometry can be related to planar T1 transitions by exchanging the  
19 concepts of space and time, this result reinforces the idea of the existence of  
20 universal principles driving the organization of tissues.

21 From the viewpoint of the tissue energetics, both the Voronoi model and *in vivo*  
22 tubes, identify the surface tension energy as the main cause of scutoids appearance  
23 and hints at the elastic energy as an additional driver for modulating the propensity  
24 of cells to undergo apico-basal intercalations. In that context, our results suggest that  
25 the so-called ‘bare’ transition rate,  $\alpha$ , or even the energy cost required to gain  
26 additional neighbors,  $\beta(s)$ , would depend on both contributions. Related to this,  
27 previous studies about the role of fluctuations in the remodeling of cellular  
28 aggregates have shown that elastic behaviors (opposed to plastic ones) contribute to  
29 reduce the cell stress by lowering the energy barrier that cells need to jump over  
30 during cellular rearrangements (Marmottant et al., 2009).

1 In our study we have found that in real tissues (both wt and mutant) the value of  
2  $\beta(s)$  is larger than in Voronoi models. We hypothesize that it is due to the purely  
3 geometrical description used in the latter. In the *in silico* model the apico-basal  
4 intercalations develop as a result of a topological constraint (a Voronoi tessellation)  
5 that we have shown describes appropriately the geometrical and packing properties  
6 of tubular epithelia. However, in the salivary glands, on top of that constraint, the  
7 cells must actively remodel their membranes and cytoskeleton to make the  
8 transitions possible. In that context, the cytoskeleton, adhesion molecules, and  
9 cellular membranes are responsible for the biophysical properties of epithelia  
10 including their energetics (Gómez-Gálvez et al., 2021b). Thus, to challenge the  
11 proposed biophysical model we measured the value of  $\beta(s)$  in salivary glands where  
12 the amount of the adhesion molecule E-cadh was reduced. Since the 3D connectivity  
13 necessarily increases with the surface ratio, the lower effective surface ratio of the  
14 mutant gland should correspond with a reduction of the 3D connectivity. However,  
15 our results show that wt and mutant glands present the same value of  $\langle n_{3D}(s_b) \rangle$   
16 (**Table S1, Fig. S7**), thus indicating that the decrease of adhesion facilitates the  
17 appearance of apico-basal intercalations. In terms of the tissue energetics, these  
18 results suggest a reduction of the energy barrier required to undergo apico-basal  
19 intercalations in the mutant glands. This prediction was confirmed by the biophysical  
20 model that provided a lower  $\beta(s)$  in the mutant case compared with the wt.

21 As for the technical advances associated to our work, we point out that a high level  
22 of detail is necessary to quantify the apico-basal intercalation phenomenon and to  
23 compare the *in vivo* data with computational models (Gómez-Gálvez et al., 2021a).  
24 Along these lines, the importance of a realistic analysis of 3D cell-cell contacts has  
25 been highlighted by recent studies focused on understanding the growth of mouse  
26 embryonic lung explants (Gómez et al., 2021) and the early development of *C.*  
27 *elegans* (Cao et al., 2020) and Ascidians (Guignard et al., 2020). Our novel  
28 methodological pipeline (**STAR Methods**) allows to implement the accurate 3D  
29 reconstruction of cells in epithelia subjected to curvature. This analysis makes  
30 possible to quantify how different packing properties, e.g., intercalations, depend on  
31 the apico-basal coordinate. These technical improvements are necessary to extract

1 biological consequences about the cellular and mechanical basis of self-organization  
2 in curved tissues (Ambrosini et al., 2017; Hirashima and Adachi, 2019; Inoue et al.,  
3 2019) or even whole embryos (Shahbazi et al., 2019).

4 As for the broader implications of our findings, our results provide new biological  
5 insight into the regulation of cell-cell connectivity in curved tissues. This property  
6 ultimately regulates juxtacrine signaling, and is pivotal for early development,  
7 primordia patterning, and cell fate determination (Guignard et al., 2020; Sharma et  
8 al., 2019; Tung et al., 2012). Moreover, recent research has shown that cellular  
9 connectivity regulates the viscosity of tissues (Petridou et al., 2021).

10 Therefore, our findings open new ways to draw implications about primary  
11 developmental processes in which epithelial bending is essential such as  
12 tubulogenesis, gastrulation, neurulation, and early embryo development. In addition,  
13 we argue that, while our analyses focus on static tissues, our results could also be  
14 relevant to understand active 3D tissue remodeling. Dynamic changes of  $\beta(s)$  would  
15 modify the apico-basal intercalation propensity and therefore the material-like  
16 properties: the larger  $\beta(s)$  the more solid-like the tissue would behave.

17 Recent studies have confirmed that adhesion-dependent active remodeling can be  
18 connected to an increased activity of neighbor exchanges. In particular, loss of  
19 function mutants of N-cadherin in the presomitic mesoderm of the zebrafish embryo  
20 cause an increase in extracellular spaces and a solid-fluid jamming transition  
21 (Mongera et al., 2018). In addition, it has been recently shown that the stabilization  
22 of E-cad at the cellular junctions in the *Drosophila* eye drives an increase of tension  
23 that can be transmitted across the tissue (Founounou et al., 2021). This tension  
24 results in a reinforcement of the solid-like tissue behavior. The salivary glands  
25 experiments confirm that a reduction of E-cadherin increases the apico-basal  
26 intercalation propensity. Our biophysical model predicted that such an increase of  
27 the apico-basal intercalation propensity must be correlated with a decrease of the  
28 energy barrier  $\beta(s)$ . Notably, this prediction was confirmed through the biophysical  
29 analyses of the  $\Delta E_{cad}$  samples.

30 Finally, with respect to the applicability of our results to other areas, we expect that  
31 the emerging field of organoids will benefit from our discoveries. A precise

1 quantification of the 3D connectivity could then help to understand the lack of  
2 reproducibility in organoid production, one of the biggest challenges of the field  
3 (Clevers, 2016; Huch et al., 2017; Schutgens et al., 2019). Also, from a medical point  
4 of view, it has been recently shown that tissue curvature affects tumor progression  
5 due to the imbalance of tensions in apical and basal surfaces of epithelial tubes  
6 (Messal et al., 2019). Our study explains how cell energetics affect the 3D packing of  
7 these cells and therefore may shed light on the mechanism of tumorigenic  
8 morphogenesis in tubular organs.

9

## 10 **ACKNOWLEDGMENTS**

11 L.M.E., P.V.-M. and P.G.-G. has been supported by the Ramón y Cajal program  
12 (PI13/01347); L.M.E., P.V.-M. and P.G.-G. work is funded by the Ministry of Economy,  
13 Industry and Competitiveness grant BFU2016-74975-P co-funded by FEDER funds,  
14 and by the Spanish Ministry of Science and Innovation Ministry of Science through  
15 grant PID2019-103900GB-I00. A.T. is funded by a “Contrato predoctoral PIF” from  
16 Universidad de Sevilla. L.M.E. and J.A.A.-S. work is funded by the Junta de Andalucía  
17 (Consejería de economía, conocimiento, empresas y Universidad) grant PY18-631 co-  
18 funded by FEDER funds. I.A.-C. would like to acknowledge the support of the 2020  
19 Leonardo Grant for Researchers and Cultural Creators, BBVA Foundation, and also  
20 the University of the Basque Country UPV/EHU grant GIU19/027. S.A. and J.B. have  
21 been supported by a Faculty Innovation Grant (FIG) by Lehigh University JB-FIG-2019.  
22 J.B. also acknowledges financial support from the Spanish Ministry of Science and  
23 Innovation through grant PID2019-105566GB-I00 and from the *LifeHUB* Research  
24 Network (CSIC).

25

## 26 **DECLARATION OF INTERESTS**

27 The authors declare no competing interests.

28

29

1 **FIGURE TITLE AND LEGENDS**

2 **Box**

3 **A: Scutoids** are prismatic-like geometric solids bounded between two surfaces (top  
4 and bottom). Scutoids are characterized by three main properties: i) The shape of  
5 their top and bottom bases, and of every parallel section between them, are  
6 polygons. ii) The lateral surfaces of scutoids can be concave and/or convex surfaces  
7 such that a set of scutoids can be packed together (laterally) without leaving any  
8 empty space. iii) Scutoids have at least one vertex along the top-bottom axis such  
9 that when packed together there are changes in the nearest-neighbors relationship.  
10 The example shows a scheme of a stereotypical scutoid (left) and four scutoids  
11 packed together (right).

12 **B: A T1-transition** is a tissue rearrangement observed in epithelial surfaces where a  
13 4-cells' motif swaps nearest neighbors along time. T1-transitions enable tissue  
14 plasticity through cellular reorganizations that lead, for example, to elongation in  
15 developing tissues.

16 **C: An apico-basal transition**, aka an **apico-basal intercalation**, is a tissue  
17 rearrangement along the apico-basal (top-bottom) axis of cells that lead to new  
18 cellular contacts (nearest-neighbors exchange). An apico-basal transition is similar to  
19 the T1-transition but instead of developing along the time it does along space.

20 **D: A 2D tessellation** (aka a 2D mosaic) is a partition of a surface with tiles that do not  
21 overlap or leave any gaps. In this example, the tiles are octagons and squares.

22 **E: A 2D Voronoi diagram** is a particular type of tessellation built by convex polygons  
23 (Voronoi cells). These polygons emerge from a set of generator seeds (black points),  
24 such that each cell contains the region that is closer to its generating seed. The so-  
25 called **Lloyd's algorithm** makes the seeds of a Voronoi diagram to converge  
26 progressively to the centroids (blue points): once a Voronoi diagram is obtained for a  
27 set of seeds (black Voronoi diagram,  $V_N$ ), an iteration of the Lloyd's algorithm  
28 consists in repeating the Voronoi tessellation by replacing the seeds by the centroids  
29 of the Voronoi tiles (blue Voronoi diagram,  $V_{N+1}$ ). The Lloyd's algorithm makes the

1 Voronoi diagram progressively more ordered in terms of the polygonal distribution of  
2 the Voronoi cells.

3 **F:** The **surface tension energy** is related to the cell-cell adherence through their  
4 lateral area contacts. For each cell, the surface tension energy reads,  $E_A = \Lambda A$ , where  
5  $\Lambda$  and  $A$  are the effective surface tension parameter and the cellular lateral area  
6 respectively. Thus, the average surface tension energy of cells reads  $\langle E_A \rangle = \Lambda \langle A \rangle =$   
7  $E_{\langle A \rangle}$  and is independent of the fluctuations of  $A$ .

8 **G:** The **contractile energy** is related to the polarized cortex activity of epithelia cells  
9 at the apical surface. The contractile energy reads  $E_L = \Gamma L^2$ , where  $L$  stands for the  
10 cellular perimeter at the apical surface and  $\Gamma$  is the cortical tension energy per unit of  
11 cell apical area. As a result, the average cell apical contractile energy increases with  
12 the fluctuations of the apical perimeter:  $\langle E_L \rangle = \Gamma \langle L^2 \rangle = E_{\langle L \rangle} + \Gamma \sigma_L^2$  where  
13  $\sigma_L^2 = \langle L^2 \rangle - \langle L \rangle^2$  is the cellular apical perimeter variance.

14 **H:** The cell **elastic energy** is related to the volume conservation of cells. The cell  
15 elastic energy reads,  $E_V = \frac{Y}{2} (V - V_0)^2$ , where  $Y$  is proportional to the Young  
16 modulus (a quantification of the relationship between the cellular stress and strain)  
17 and,  $V$  and  $V_0$  represent the *actual* and target cellular volumes respectively. The  
18 average elastic energy per cell increases with the fluctuations of the volume:  
19  $\langle E_V \rangle = \frac{Y}{2} \langle (V - V_0)^2 \rangle = E_{\langle V \rangle} + \frac{Y}{2} \sigma_V^2$  where  $\sigma_V^2 = \langle V^2 \rangle - \langle V \rangle^2$  is the cellular volume  
20 variance.

21

22

1 **Figure 1. *In silico* Voronoi epithelial model: energetics and analysis of apico-basal**  
2 **cell intercalations in tubes**

3 **A:** (left) Scutoids entail apico-basal intercalations among packing cells that can be  
4 envisioned as *spatial* T1 transitions to exchange neighbors (right): the green and the  
5 red cells are neighbors in the basal surface (but not in the apical surface) while the  
6 opposite is true for the blue and the yellow cells. **B:** *In silico* Voronoi 3D epithelial  
7 models are generated by populating with cell seeds (circles) the apical surface,  $\Sigma_a$ .  
8 The location of cell seeds at any other surface/plane,  $\Sigma$ , is obtained by implementing  
9 apical normal projections,  $\mathbf{n}$ , up to the basal surface,  $\Sigma_b$ . At each surface,  $\Sigma$ , a 2D  
10 Voronoi tessellation is performed and the 3D cellular shape of the cell is built upon  
11 the collection of these tessellations. **C:** (top) In the particular case of tubular  
12 epithelia, normal projections of apical cell seeds correspond to radial projections, and  
13 the thickness/curvature of tubes are characterized by the surface ratio,  $s = R/R_a$   
14 (apical/basal surfaces: light/dark blue.  $R$ : dashed yellow). (bottom) Illustrative  
15 rendering of a Voronoi tube cell. **D:** The so-called CVT scale (iterations of Lloyd's  
16 algorithm, **STAR Methods**) measures the topological disorder in *in silico* tubular  
17 epithelia and leads to different cellular morphologies. In a V1 (Voronoi 1) model cell  
18 seeds are randomly distributed on the apical surface to generate a planar Voronoi  
19 tessellation (**STAR Methods**). By applying the Lloyd algorithm iteratively, the apical  
20 topological disorder diminishes (top to bottom: V1, V5, and V10 examples). The  
21 random location of seeds in V1 implies the emergence of a wide range of different  
22 polygonal cell types. As Lloyd's algorithm iterates, the larger the tessellation order is  
23 (**Box E**). We observe this progressive ordering from a V1 to V10 as polygonal  
24 distributions converge to results with a larger proportion of hexagons and a  
25 reduction of the other polygonal shapes (inset: polygon distribution insets for V1, V5,  
26 and V10). The average number of apico-basal intercalations per cell in *in silico* tubes  
27 ( $n = 20$  realizations per CVT scale, each tube composed by 200 cells) increases with  
28 the tissue thickness (surface ratio) but does not change significantly with the CVT  
29 scale. The black/red/green arrows correspond to the illustrative examples of the  
30 planar apical tessellations shown on the left. **E:** The average lateral cell area as a  
31 function of the CVT and the surface ratio (values normalized to the V1 case at  
32  $s_b = 10$ ,  $n = 20$  per CVT scale) indicates that the average surface tension energy

1 does not depend on the level of topological disorder. **F:** Average (green bar) and  
2 standard deviation (red lines) of the apical cellular perimeter as a function of the CVT  
3 scale. Values normalized with respect to the V1 case ( $n = 20$  per CVT scale). **G:** The  
4 cellular volume variance is a proxy for the average elastic cell energy (**STAR**  
5 **Methods**). The latter decreases with the CVT scale and increases with the surface  
6 ratio (tissue thickness) ( $n = 20$  per CVT scale). Volume values were normalized with  
7 respect to the V1 case with  $\langle V(s_b = 10) \rangle = 1$ . **H:** Cross-correlation between average  
8 energy profiles along the apico-basal axis,  $\langle E_A \rangle$  (dark grey),  $\langle E_V \rangle$  (red), and  $\langle E_A \rangle +$   
9  $\langle E_L \rangle$  (light grey), and the number of apico-basal intercalations,  $\langle i \rangle$ . Solid lines stand  
10 for the averages among disorder configurations (i.e., CVT scale) and the dotted lines  
11 delimit the standard deviation band.  $\langle E_V \rangle + \langle E_L \rangle$  has not been plotted since the extra  
12 contribution of the contractile term,  $\langle E_L \rangle$ , does not modify the correlation function. **I:**  
13 Cross-correlation between energy gradients ( $\partial_s \langle E_A \rangle$  and  $\partial_s \langle E_V \rangle$ ) and the gradient of  
14 intercalations along the apico-basal axis ( $\partial_s \langle i \rangle$ ). Color code as in **H**.

1 **Figure 2. Three-dimensional packing and connectivity properties of the Voronoi**  
2 **tubular model**

3 **A:** (left) Schematic representation of a 3D histogram that accounts for the probability  
4 that cells have  $n_a$  (number) of neighbors in the apical surface and  $n_b$  neighbors in the  
5 basal surface. Cells with the same polygonal class in apical and basal surfaces  
6 contribute to bins along the diagonal (red squares). The bins spreading away from  
7 the diagonal (green squares) ensures the presence of scutoidal cells. E.g.: the red and  
8 green cells shown in the plot contribute to the bins indicated in the 3D histogram  
9 (red and green stars respectively). (right) 3D histograms of V5 tubes for increasing  
10 values of the surface ratio. A larger value of the spreading coefficient,  $\eta^2$ , (**STAR**  
11 **Methods**) indicates an increasing number of scutoids. **B:** Density plot showing the  
12 value of the spreading coefficient,  $\eta^2$ , of 3D histograms as a function of the surface  
13 ratio and the Voronoi class in *in silico* tubes ( $n = 20$  tubes per CVT scale). **C:** Cross-  
14 correlation between average energy profiles along the apico-basal axis,  $\langle E_A \rangle$  (dark  
15 grey),  $\langle E_V \rangle$  (red), and  $\langle E_A \rangle + \langle E_L \rangle$  (light grey), and the spreading coefficient,  $\eta^2$ . Solid  
16 lines stand for the averages among disorder configurations (i.e., CVT scale) and the  
17 dotted lines delimit the standard deviation band. .  $\langle E_V \rangle + \langle E_L \rangle$  has not been plotted  
18 since the extra contribution of the contractile term,  $\langle E_L \rangle$ , does not modify the  
19 correlation function.

1 **Figure 3. *Drosophila's* salivary gland analysis**

2 **A:** (top) Full projection of a wildtype salivary gland (cell contours stained by Cy3-  
3 labeled phalloidin, **STAR Methods**). (middle) Computer rendering of the segmented  
4 salivary gland shown on top. Scale bar  $100\mu m$ . (bottom) 3D rendering of a  
5 representative segmented salivary gland. **B:** Density plot of the 3D distribution of  
6 neighbor exchanges between apical and basal surfaces as a function of the number of  
7 neighbors in apical,  $n_a$ , and basal,  $n_b$ , surfaces (as in **Fig. 2A**) in wildtype salivary  
8 glands ( $n = 20$  glands, 979 cells). **C:** Average profiles of the number of apico-basal  
9 intercalations,  $\langle i \rangle$ , average lateral area,  $\langle A \rangle$ , and cellular volume fluctuations,  $\sigma_V^2$  in *in*  
10 *vivo* tubes as a function of the apico-basal coordinate,  $s$  ( $n = 20$  glands, similar to  
11 **Fig. 1D-E, G**). **D-E:** Cross-correlation analysis between energy and intercalation  
12 profiles (same as **Fig. 1H-I**). The error band indicates in this case the variability among  
13 experimental samples ( $n = 20$  glands).

1 **Figure 4. Biophysical model: *in silico* and *in vivo* results**

2 **A:** (top) Cell intercalations along the apico-basal axis can be visualized as spatial T1  
3 transitions (non-reversible: once a neighbor is won it cannot be lost). (bottom) The  
4 “poor get richer” principle (**STAR Methods**) suggests an increasing energetic cost  
5 (i.e., a larger activation energy) for recruiting new neighbors as a function of the  
6 number of neighbors already won. In our model,  $\beta(s)$  accounts for the energetic cost  
7 per 3D neighbor (per apico-basal intercalation) to recruit a new neighbor (**STAR**  
8 **Methods**). **B:** The energy landscape shown in **B** (bottom) can be modeled by a  
9 stochastic dynamics (a Kolmogorov rate equation) where cells increase their 3D  
10 neighbors with a probability per unit of surface ratio,  $r_{n,m}$ , that depends on the  
11 activation energy,  $\beta(s)$ , a ‘bare’ transition rate,  $\alpha$ , and the maximum cell  
12 connectivity  $N_{max}$  (**STAR Methods**). **C:** Results of the Kolmogorov model in V8  
13 ( $s_b = 1.75$ ) *in silico* tubes ( $n = 20$ ). The left/center density plots represent the  
14 cellular connectivity distribution (i.e., the fraction/probability of cells with a given  
15 number of 3D neighbors) as a function of  $s$  obtained in the Voronoi simulation (left)  
16 and as predicted by the Kolmogorov model (center); the red circles (left/right)  
17 indicate the average number of 3D neighbors per cell  $\langle n_{3D} \rangle$ ; the red line  
18 (center/right) shows  $\langle n_{3D} \rangle$  as obtained by the Kolmogorov model. The density plot on  
19 the right shows the difference between the predicted and the actual connectivity  
20 distributions and the corresponding error,  $\varepsilon^2$  (magenta lines). **D:** Same as panel **C** but  
21 results obtained in salivary glands ( $n = 20$  glands). The maximum value of  $s$  in the  
22 analyzed radial sections of the glands is  $s = 6.5$ . This value being the largest radial  
23 section of the smallest gland (**STAR Methods**).

1 **Figure 5. Biophysical analysis of  $\Delta$ Ecad salivary glands**  
2 **A:** (top) Full projection of a  $\Delta$ Ecad salivary gland (cell contours stained by Cy3-labeled  
3 phalloidin, **STAR Methods**). (bottom) Computer rendering of the mutant salivary  
4 gland shown on top. Scale bar  $100\mu m$ . **B:** Results of the Kolmogorov model for the  
5  $\Delta$ Ecad salivary gland ( $n = 10$  glands). The left/center density plots represent the  
6 connectivity distribution (i.e., the fraction/probability of cells with a given number of  
7 3D neighbors) as a function of  $s$  obtained in the Voronoi simulation (left) and as  
8 predicted by the Kolmogorov model (center); the red circles (left/right) indicate the  
9 average number of 3D neighbors per cell ( $\langle n_{3D} \rangle$ ); the red line (center/right) shows  
10  $\langle n_{3D} \rangle$  as obtained by the Kolmogorov model. The density plot on the right shows the  
11 difference between the predicted and the actual connectivity distributions and the  
12 corresponding error,  $\varepsilon^2$  (magenta lines). Same color code than in **Fig 4C-D**. The  
13 maximum value of  $s$  in the analyzed radial sections of the glands is  $s = 5.5$ . This  
14 value being the largest effective radial section of the smallest gland (**STAR Methods**).  
15 **C:** Energy cost required to gain additional neighbors as a function of  $s$  (**STAR**  
16 **Methods**) for wt glands (green), for  $\Delta$ Ecad glands (red), and for the V8 ( $s_b = 1.75$ )  
17 model (blue). The inset shows the values of the bare transition rates,  $\alpha$ , and the  
18 average value (along the apico-basal coordinate) of  $\beta$ .

## 1 STAR METHODS

### 2 Immunohistochemistry and confocal imaging of salivary glands

3 Flies were grown at 25 °C using standard culture techniques. The following lines  
4 were used: *Oregon R (wt)*, *UAS-shg-RNAi* (BL38207), *AB1-Gal4* (BL1824). *AB1-Gal4*  
5 drives Gal4 protein in the third instar larva salivary gland. We dissected the salivary  
6 glands from third instar larvae. After PBS dissection, the glands were fixed using 4%  
7 paraformaldehyde in PBS for 20 min. The samples were washed three times for 10  
8 min with PBT (PBS, 0.3% Triton) and then incubated for 1 hr 45 minutes at room  
9 temperature with Cy3-labeled phalloidin (Sigma) to label the cell contours of the  
10 epithelial cells. Stained larval salivary glands were mounted using Fluoromount-G  
11 (Southern Biotech). We used two pieces of double-sided adhesive tape (one on top of  
12 each other) as a spacer (Aldaz et al., 2013), so the salivary glands preserve their  
13 shape. Images were taken using a Nikon Eclipse Ti-E laser scanning confocal  
14 microscope. The images were captured using a ×20 dry objective and 2.5 μm steps  
15 between slices. The image stacks were exported as 1024 × 1024 pixels TIFF files.

16

### 17 Quantification of fluorescence intensity

18 The E-cadherin fluorescence intensity was measured in Fiji by using the Plot Profile  
19 tool. We used 3 wt and 3 ΔEcad representative glands, taking 10 individual  
20 measurements for each sample (**Fig. S7**). We used rectangular ROIs to measure the  
21 intensity profiles of lateral cell membrane in the Z-depth where the lumen was  
22 visible. In this way, we were able to capture the whole lateral cell membranes from  
23 apical to basal. To ensure, a high-quality detection of the cell membrane we  
24 developed a maximum Z-projection of those Z-slices where the cell outline of interest  
25 and the lumen are clearly visible. Note that the output of the Plot Profile is a 2D plot  
26 that displays a “column average plot”, where the *X* axis represents the horizontal  
27 distance through the selection (apico-basal cell outline) and the *Y* axis the vertically  
28 averaged pixel intensity.

29

### 1     **3D glands segmentation**

2     To segment the salivary gland stacks of images and reconstruct (semi-automatically)  
3     the shape of cells in three dimensions we used the Fiji (Schindelin et al., 2012) plugin  
4     LimeSeg (Machado et al., 2019). It infers cell outlines by using surface elements  
5     (“Surfels”) obtained by manually placing single ellipsoidal-like seeds on every cell (see  
6     <https://imagej.net/LimeSeg> for details). Once cell outlines were found, we exported  
7     them as point clouds (output). We developed a custom-made Matlab code (2021a  
8     MathWorks) to postprocess the output of LimeSeg in order to correct errors and  
9     obtain perfectly segmented salivary glands. In addition, we manually segmented the  
10    lumen of the glands using the Volume Segmenter app, in Matlab. To faithfully  
11    represent the gland as a cylinder, we selected a subset of cells: cells that were not  
12    ductal, neither located at the tip of the gland.

13    To segment mutant salivary glands we took advantage from the 20 segmented wt  
14    salivary glands, and we used them as training dataset into a deep-learning  
15    segmentation pipeline. We trained a stable 3D-U-Net CNN ((Franco-Barranco et al.,  
16    2021), [https://github.com/danifranco/EM\\_Image\\_Segmentation](https://github.com/danifranco/EM_Image_Segmentation)) using as input the  
17    salivary glands phalloidin channel (actin filaments) staining cell outlines, and as target  
18    the segmented cell outlines. The output (prediction) of this pipeline was a probability  
19    map of cell outlines, that was post-process using the PlantSeg (Wolny et al., 2020)  
20    segmentation module to extract individual instances. Here, again, we segmented the  
21    lumen of the glands using the Volume Segmenter app, and segmentation errors were  
22    curated using our custom-made Matlab code.

23    To obtain the cellular neighborhood relations of salivary glands for different values of  
24    the radial expansion, we proceeded as follows. We calculated the cell height by  
25    estimating the distance between the centroid of the cell apical surface with respect  
26    to the centroid position of its basal surface,  $d(s_a, s_b)$ . Then, to capture a concentric  
27    radial section of the gland, we linearly extrapolated the equivalent cell height to the  
28    given surface ratio,  $s$ :

$$29 \quad d(s_a, s) = d(s_a, s_b) \frac{s}{s_b} \quad (2)$$

1 where  $d(s_a, s)$  is the Euclidean distance between the position of the centroid of the  
2 cell at the apical surface,  $s_a = 1$ , and the position of the centroid at a value  
3  $s = R/R_a$  of the radial expansion. Finally, to obtain the gland cylindrical radial  
4 section for a given value of the radial expansion,  $s$ , we collected all voxels between  
5 apical and the upper bound of the calculated distance  $d(s_a, s)$ .

6

## 7 **Salivary glands measurements**

8 We quantified the following geometrical and topological/connectivity descriptors of  
9 the segmented salivary glands using a custom-made Matlab code:

- 10 - Surface ratio ( $s$ ): Assuming a cylindrical shape for glands, we estimated  $s$  by  
11 measuring the minimum distance between each cell apical centroid and  
12 lumen skeleton ( $R_a$ ), and measuring  $h$ , the distance between apical cell  
13 centroid and cell centroid of an outer cell layer (i.e., basal surface or a  
14 concentric layer between apical and basal). Being, the individual surface ratio  
15 of a cell,  $s_{cell} = \frac{R_{a_{cell}} + h_{cell}}{R_{a_{cell}}}$ , we averaged all the individual cell measurements  
16 to calculate the representative  $s$  value corresponding to a gland,  $s = \langle s_{cell} \rangle$ .
- 17 - Cell apical perimeter, lateral surface area, and the cellular volume.
- 18 - Number of cell contacts: we measured the number of cell neighbors of each  
19 cell surface, that is, apical, basal or lateral. In order to remove artefacts, 2  
20 cells must share at least 0.5% of their lateral surfaces area to enable them to  
21 be considered as neighbors.  $n_a$ ,  $n_b$ , and  $n_{3D}$  of each gland were calculated  
22 after averaging the number of cells neighbors along the gland.
- 23 - Percentage of scutoids, average of apico-basal transitions. We quantify the  
24 percentage of scutoidal cells that conform the gland and the number of apico-  
25 basal transitions in which each cell is involved.

26

27 All the measurements were carried along different concentric radial sections of the  
28 glands. We captured the gland thicknesses starting at the apical surface ( $s_a = 1$ ) and  
29 increasing progressively the surface ratio by  $\Delta s = 0.5$ , until reaching the basal  
30 surface ( $s_b$ ). In this way, the number of the captured radial sections will depend on

1 the  $s_b$  value of each gland. To compare the glands of each phenotype (either wt or  
2 mutant) in terms of connectivity related with the surface ratio, we used a maximum  
3 radial section common to all the glands.

4 In  $\Delta Ecad$  mutant glands, due to their phenotype (cells bulge at the basal surface),  
5 we removed the bulging tips of cells to quantify the *effective* surface ratio  $s^*$ : the  
6 maximum value of the surface ratio up to which cells are contacting (that is,  
7  $1 \leq s \leq s^* \leq s_b$ ). We noticed that the 3D connectivity of cells is not modified by this  
8 approach. To remove the volume of cell tips, we captured all lateral and apical  
9 surfaces of cells and we filled each cell volume using the *alphaShape* Matlab function.

10

### 11 **Voronoi tubular model**

12 Using custom-made Matlab code we generated a Voronoi model that simulates the  
13 surface of a cylinder unfolded over the Cartesian plane, see details in Gomez-Galvez  
14 et al. ((Gómez-Gálvez et al., 2018), **Methods**). The only difference with the cited  
15 methodology, is that in this work the Voronoi diagrams has been constructed by  
16 means of the Delaunay triangulation technique. Therefore, we just considered the  
17 cells' vertices information (Cartesian coordinates and connections) for a much faster  
18 computation. For each realization, we used an initial set of 200 randomly located  
19 seeds on a rectangular domain of 512 (X axis; transverse axis of cylinder) per 4096 (Y  
20 axis; longitudinal axis of cylinder). We performed this procedure for 10 different  
21 initial Voronoi diagrams (Voronoi 1 (V1, random seeds) to Voronoi 10 (V10, more  
22 ordered and homogeneous cells). These diagrams represent the apical (inner)  
23 surfaces of computational tubes, and they were obtained by applying N-1 times the  
24 Lloyd's algorithm (Lloyd, 1982) to the random seeds, where N is then the resulting  
25 Voronoi model. For instance, to compute a V1, we use purely random seeds, while to  
26 obtain a V4 diagram, it would be required to apply 3 times the Lloyd's algorithm to  
27 random seeds. In the limit of the CVT scale (iterations of the Lloyd's algorithm) going  
28 to infinity the organization of cells tends to a hexagonal lattice. Subsequent radial  
29 sections that define computational tubes with different surface ratios were obtained  
30 by implementing a radial projection of the Voronoi seeds. For each apical surface of  
31 the tube, we generated 40 expansions by incrementing the surface ratios ( $s_b$ ) using

1 0.25 steps: 1 (apical), 1.25, 1.5, ... ,10 (19  $s$ -steps  $\times$  10 apical cell arrangements  $\times$  20  
2 realizations).

3 As for the 3D reconstruction of cells in Voronoi tubes, each set of seeds that  
4 characterizes cells on a given cylindrical section defines a unique 2D Voronoi diagram  
5 at every surface and hence the corresponding 2D cellular domains. The set of 2D  
6 Voronoi regions that belong to the same radially projected seed from the apical to  
7 the basal surface then define each 3D cellular shape. Each of the obtained 3D cells  
8 was further processed using the Matlab function '*alphaShape*' to transform the set of  
9 voxels into a compact, solid, object. This reconstruction pipeline was implemented  
10 using Matlab (2021a).

11 As for the connection of the CVT scale with the average elastic energy of cells, we  
12 first notice that for a given tube of length  $L$ , radiuses  $R$  and  $R_a$ , and with a fixed  
13 number of cells,  $N$ , the average cell volume,  $\langle V \rangle$ , is independent of the CVT scale:

14  $\langle V \rangle = \frac{1}{N} \sum_{i=1}^N V_i = \pi L(R^2 - R_a^2)/N = \pi L R_a^2 (s^2 - 1)/N$ . On the other hand, if cells

15 have a target volume  $V_0$  then the elastic energy (linear regime) of cell  $i$  reads

16  $E_{V_i} = \frac{Y}{2} (V_i - V_0)^2$ , where  $Y$  is proportional to the Young's modulus. Consequently,

17 the average cell elastic energy,  $\langle E_V \rangle = \frac{1}{N} \sum_{i=1}^N E_{V_i} = E_{\langle V \rangle} + \frac{Y}{2} \sigma_V^2$ , where  $E_{\langle V \rangle} =$

18  $\frac{Y}{2} (\langle V \rangle - V_0)^2$  is the elastic energy of a cell with an average cell volume  $\langle V \rangle$  and

19  $\sigma_V^2 = \langle V^2 \rangle - \langle V \rangle^2$  is the variance of the cellular volume (the cell size fluctuations).

20 Since  $E_{\langle V \rangle}$  is independent of the CVT scale and  $\sigma_V^2$  decreases with the CVT scale (i.e.,  
21 as the tissue becomes more ordered) then the average elastic cell energy necessarily

22 decreases as the CVT increases. In our simulations and experiments the cellular  
23 volume is computed by using the value of cell area sections  $\mathcal{A}(s)$  as a function of the

24 surface ratio,  $s$ . Specifically, we used the trapezoidal rule,  $V(s) = \int_{z=s_a}^{z=s} \mathcal{A}(z) dz \approx$

25  $\frac{\Delta s}{2} [\mathcal{A}(s_a) + 2\mathcal{A}(s_a + \Delta s) + \dots + 2\mathcal{A}(s_a + (n-1)\Delta s) + \mathcal{A}(s_a + n\Delta s)]$ . Where

26  $s_a + n\Delta s = s$  and  $\Delta s = 0.25$ . Cell volumes were normalized considering Voronoi 1

27 tubes from CVT scale as reference, such its average cell volume will represent the

28 unity  $\langle V(s_b = 10) \rangle = 1$ . Likewise, for estimating the surface lateral area we used the

29 trapezoidal rule using the value of the cellular perimeter,  $L(s)$ , that is:  $A(s) =$

1  $\int_{z=s_a}^{z=s} L(z) dz \approx \frac{\Delta s}{2} [L(s_a) + 2L(s_a + \Delta s) + \dots + 2L(s_a + (n-1)\Delta s) + L(s_a +$   
2  $n\Delta s)]$ . Besides, we normalized the lateral surface area following the same criterion  
3 than with volumes. Additionally, we proceed in a similar way to estimate the cellular  
4 lateral area and volume as a function of  $s$  in salivary glands.

5

## 6 **Cross-correlation definition**

7 Dimensionless cross-correlation,  $C(s)$ , between  $X(s)$  (e.g.  $\langle E_A(s) \rangle$ ) and  $Y(s)$  (e.g.  
8  $Y(s) = \langle i(s) \rangle$ ) is defined as follows:  $C(s) = \frac{1}{N} \sum_{s'} X(s') Y(s + s')$  where  $N =$   
9  $(\sum_{s'} X(s')^2 \sum_{s'} Y(s')^2)^{1/2}$  is a normalization constant such that the auto-  
10 correlation becomes one (at maximum) at zero lag. When required, spatial  
11 derivatives were estimated as  $\partial_s F(s) = \frac{F(s+\Delta s) - F(s)}{\Delta s}$ .

12

## 13 **Voronoi tubular model measurements.**

14 We measured the following properties of cells in Voronoi tubular models: area,  
15 perimeter and number of sides of cells for a given radial section, and total number  
16 neighbors. Additionally, we computed the percentage of scutoids, the number of  
17 apico-basal transitions, the polygon distribution of every surface (radial sections). In  
18 these quantifications, we disregarded cells at the boundaries (tips of tubes) to avoid  
19 'border effects'.

20

## 21 **Relation between total accumulated 3D neighbors and the number of** 22 **intercalation events**

23 Scutoids have a Euler characteristic  $\chi = 2$  such that  $V - E + F = 2$ , where  $V$ ,  $E$ ,  
24 and  $F$  accounts for the number of vertexes, edges, and faces respectively. We  
25 assumed that the apical,  $a$ , and basal,  $b$ , faces of scutoids tessellating a cylindrical  
26 space have radial coordinates  $R_a$  and  $R_b$  respectively. Then, for any value of the  
27 surface ratio expansion,  $s = R/R_a$ , these solids can be mapped into a connected  
28 plane graph with the same Euler characteristic (a sort of projection of the vertexes  
29 and connectors into the plane, see **Fig. S10**). Thus, as a function of  $s$ , the accumulated

1 number of 3D neighbors reads  $n_{3D}(s) = E(s) - V(s)$ . Since in tubular geometries  
 2 the radially projected seeds from the apical to the basal surface never come closer,  
 3 as  $s$  increases (i.e., apico-basal intercalations are not reversible).

$$4 \quad n_{3D}(s) = \max(\{V(s)\}) = \min(\{V(s)\}) + i(s) \quad (3)$$

5 where  $\{V(s)\} = \{V(1), V(1 + ds), \dots, V(s_b)\}$  and  $i(s)$  denotes the number of  
 6 intercalation points in the interval  $s \in [1, s_b]$ . In the case of a 3D tessellation with  $N$   
 7 cells, where  $M$  of them do not show any intercalation, the total number of  
 8 accumulated neighbors reads,

$$9 \quad n_{3D}(s) = \sum_{j=1}^N n_{3D}^{(j)}(s) = \sum_{j=1}^M V^{(j)}(1) + \sum_{j=1}^{N-M} \max(\{V^{(j)}(s)\}) = \\ 10 \quad \sum_{j=1}^M V^{(j)}(1) + \sum_{j=1}^{N-M} \{\min(\{V^{(j)}(s)\}) + i^{(j)}(s)\} \quad (4)$$

11 Given that each intercalation point is shared by four cells, two of them necessarily  
 12 increase their number of vertices in a given  $s$ -plane and two of them decrease their  
 13 number of vertices. Thus, in the case of a decrease  $\max(\{V^{(j)}(s)\}) = V^{(j)}(1)$  and in  
 14 the case of an increase  $\min(\{V^{(j)}(s)\}) + i^{(j)}(s) = V^{(j)}(1) + i^{(j)}(s)$ . Consequently,

$$15 \quad n_{3D}(s) = \sum_{j=1}^N V^{(j)}(1) + \sum_{j=1}^{(N-M)/2} i^{(j)}(s) = \sum_{j=1}^N V^{(j)}(1) + \frac{1}{2} \sum_{j=1}^{N-M} i^{(j)}(s) \quad (5)$$

16 where we used the fact that for every intercalation event that increases by one the  
 17 number of neighbors there is one that decreases the number of neighbors in the  
 18 same amount; consequently, we can add up all intercalation events and divide by  
 19 two. Hence the average number of accumulated 3D neighbors,  $\langle n_{3D}(s) \rangle = n_{3D}(s)/N$   
 20 reads  $\langle n_{3D}(s) \rangle = \langle V(1) \rangle + \langle i(s) \rangle / 2$ ;  $\langle i(s) \rangle$  being the average number of apico-basal  
 21 intercalations per cell. Finally, by considering that any  $s$ -surface, and in particular the  
 22 apical surface  $s = 1$ , corresponds to a 2D tessellation of convex polygons,  $\langle V(1) \rangle = 6$   
 23 we conclude that,

$$24 \quad \langle n_{3D}(s) \rangle = 6 + \frac{1}{2} \langle i(s) \rangle \quad (6)$$

25

## 26 **The 3D neighbor's accumulation in tubular epithelia follows a "poor get richer"** 27 **principle**

28 In order to investigate additional phenomena that could help to understand how  
 29 the 3D cellular connectivity is regulated, we computed the net gain of cellular

1 neighbors in epithelial tubes as a function of the 2D polygonal cell class at the apical  
2 surface. We observed, both in the salivary glands and in the Voronoi model (in  
3 particular in the case V8 ( $s_b = 1.75$ ) that compares the best with *in vivo* glands), that  
4 the smaller the number of neighbors of a cell at the apical surface, the larger the net  
5 gain of 3D cellular contacts (**Fig. S4**). This behavior was also obtained with respect to  
6 the 2D polygonal cell class at the basal surface (**Fig. S4**). These results suggest that, in  
7 terms of the cellular packing, tubular epithelia follow a “poor get richer” principle:  
8 the less neighbors a cell has in a surface (apical or basal), the larger the net increase  
9 of 3D cellular contacts.

10

### 11 **In Voronoi tubes the net gain of 3D neighbors is bounded**

12 The “poor get richer” behavior can be justified by mathematical arguments that  
13 show that the probability to increase the cellular connectivity necessarily decreases  
14 with the number of current neighbors (**Fig. S5**). Assuming a cylindrical geometry (e.g.,  
15 epithelial tubes), each point at a given radial surface can be represented into the  
16 Cartesian plane; where coordinate  $x$  accounts for the cylindrical transversal  
17 coordinate and coordinate  $y$  for the longitudinal one (see **Fig. S5**). Thus, if the  
18 coordinates of a point (e.g., a Voronoi seed) at the apical surface are given by  $(x, y)$ ,  
19 the coordinates of that point at a surface with a value of the cylindrical radial  
20 expansion  $s \in [1, \infty)$  can be found by defining the function  $f_s: \mathbb{R}^2 \rightarrow \mathbb{R}^2$   $f_s(x, y) =$   
21  $(sx, y)$ . Under these conditions, we aim to characterize the seeds that generate  
22 scutoids (exchanges in the neighboring relations of seeds) as  $s$  changes.

23 *Lemma 1.* Given three non-colinear points  $\{A, B, C\}$  that define a circle (a nearest-  
24 neighbors relation), and another exterior point  $D$ , if  $s > 1$  exists such that  $f_s(D)$  is  
25 interior to the circle defined by  $\{f_s(A), f_s(B), f_s(C)\}$ , then  $D$  is inside of the vertical  
26 parabola containing  $\{A, B, C\}$  (**Fig. S5**).

27 *Remark.* If two of the three points  $\{A, B, C\}$  are on the same vertical line, then the  
28 parabola considered in Lemma 1 degenerates as a vertical strip. Even in this case, the  
29 thesis of the Lemma is true if we replace the interior of the parabola by the inside of  
30 the strip.

1 *Proof.* Without loss of generality, we can suppose that  $\{A, B, C\}$  are  
 2 counterclockwise oriented and that they have Cartesian coordinates  $(a_1, a_2)$ ,  
 3  $(b_1, b_2)$  and  $(c_1, c_2)$  respectively.

4 Thus, the point  $D(x, y)$  is outside the circle defined by  $\{A, B, C\}$  if, and only if, the  
 5 sign of the following determinant is negative:

$$6 \begin{vmatrix} a_1 & a_2 & a_1^2 + a_2^2 & 1 \\ b_1 & b_2 & b_1^2 + b_2^2 & 1 \\ c_1 & c_2 & c_1^2 + c_2^2 & 1 \\ x & y & x^2 + y^2 & 1 \end{vmatrix} = \begin{vmatrix} a_1 & a_2 & a_1^2 & 1 \\ b_1 & b_2 & b_1^2 & 1 \\ c_1 & c_2 & c_1^2 & 1 \\ x & y & x^2 & 1 \end{vmatrix} + \begin{vmatrix} a_1 & a_2 & a_2^2 & 1 \\ b_1 & b_2 & b_2^2 & 1 \\ c_1 & c_2 & c_2^2 & 1 \\ x & y & y^2 & 1 \end{vmatrix} < 0 \quad (7)$$

7 For the sake of simplicity, we represent the previous equation as:

$$8 \det(\mathcal{A}) = \det(\mathcal{B}) + \det(\mathcal{C}) < 0 \quad (8)$$

9 On the other hand, by considering  $x$  and  $y$  as variables, the equation  $\det(\mathcal{A}) = 0$   
 10 corresponds to the circle defined by  $\{A, B, C\}$ , and  $\det(\mathcal{B}) = 0$  corresponds to the  
 11 vertical parabola defined by the same three points. Consequently, the inequality  
 12  $\det(\mathcal{B}) > 0$  defines the locus of interior points to that parabola.

13 Now, assuming that  $s > 1$  exists such that  $f_s(D)$  is interior to the circle defined by  
 14  $\{f_s(A), f_s(B), f_s(C)\}$ . Then,

$$\begin{vmatrix} sa_1 & a_2 & s^2a_1^2 + a_2^2 & 1 \\ sb_1 & b_2 & s^2b_1^2 + b_2^2 & 1 \\ sc_1 & c_2 & s^2c_1^2 + c_2^2 & 1 \\ sx & y & s^2x^2 + y^2 & 1 \end{vmatrix} = s^3 \det(\mathcal{B}) + s \det(\mathcal{C}) > 0 \quad (9)$$

15 Or, equivalently,  $s^2 \det(\mathcal{B}) + \det(\mathcal{C}) > 0$ , so,  $s^2 \det(\mathcal{B}) > -\det(\mathcal{C})$ . If  $\det(\mathcal{B}) <$   
 16  $0$ , then  $1 < s^2 < -\frac{\det(\mathcal{C})}{\det(\mathcal{B})}$  and therefore  $\det(\mathcal{B}) > -\det(\mathcal{C})$ . The latter is in  
 17 contradiction with  $\det(\mathcal{B}) + \det(\mathcal{C}) < 0$ . As a result,  $\det(\mathcal{B}) > 0$ , and the following  
 18 inequality holds,

$$s^2 > -\frac{\det(\mathcal{C})}{\det(\mathcal{B})} > 1 \quad (10)$$

19 Notice that if the circle defined by  $\{A, B, C\}$  is surrounded by a set of points and we  
 20 change continuously the parameter  $s$  in the interval  $[1, \infty)$ , it is possible to detect the  
 21 first point touching the circle defined by  $\{f_s(A), f_s(B), f_s(C)\}$ . That point can be

1 obtained by computing all the points at  $s = \sqrt{-\frac{\det(C)}{\det(B)}}$ . Hence, the first point  
 2 contacting the circle will be that with the minimum value of  $s$ .

3 As for proving that the average of the number of neighbors of a cell induced by a  
 4 seed grows is bounded as a function of the surface ratio, we state the following  
 5 proposition:

6 *Proposition 1.* Given a Voronoi seed representing a cell, if  $n_{3D}(s)$  is the total  
 7 number of accumulated cell neighbors as  $s$  increases from  $s = 1$  (apical surface) to a  
 8 given value of  $s$ , then  $\langle n_{3D}(s) \rangle$  is a bounded function for a finite cylinder.

9  
 10 *Proof.* We model the apical surface as the cylinder  $2\pi r \times h$ , where  $r$  represents the  
 11 inner radius and  $h$  the length of the cylinder. Given a seed  $A$  in that surface, in the  
 12 corresponding Delaunay triangulation it appears as a point surrounded by triangles  
 13 defining the neighborhood of  $A$ . By Lemma 1, each triangle defines a vertical  
 14 parabola and a circle. So, any other seed touching  $A$  in other layer must be inside of  
 15 one of the parabolas and outside of all circles (see **Fig. S5**). Let's denote  $\mathcal{R}_{s,A}$  the  
 16 feasible region for a new neighbor of  $A$  in the layer represented by  $s$ , i.e., all points  
 17 inside one of the parabolas and outside all the circles. Thus, if  $\#(\mathcal{R}_{s,A})$  is the number  
 18 of seeds in that region that are not neighbors of  $A$  in the apical surface, obviously, an  
 19 upper bound to the number of new neighbors to  $A$  is given by  $\#(\mathcal{R}_{s,A}) \leq \#(\mathcal{R}_{1,A})$ .

20  
 21 On the other hand, that number of seeds is, in average, proportional to the density  
 22 of seeds times the area of  $\mathcal{R}_{s,A}$ , therefore, the average number of accumulated  
 23 neighbors of  $A$ , denoted as  $\langle n_{3D}(A) \rangle$ , will be bounded by the change of the density of  
 24 points when growing  $s$ , this is to say,

$$25 \quad d\langle n_{3D}(A) \rangle \leq M \cdot \frac{\mathcal{R}_{s,A}}{2\pi sr \cdot h} ds \quad (11)$$

26 where  $M$  represents the total number of seeds (i.e., the total number of cells that is  
 27 a constant) and the quotient is the area of  $\mathcal{R}_{s,A}$  divided by the area of a given radial  
 28 layer. In general, it is not possible to integrate equation (4), since the area of  $\mathcal{R}_{s,A}$  is  
 29 known only in very few, particular, cases.

1 In the case of a finite cylinder,  $\langle n_{3D}(A) \rangle \leq \#(\mathcal{R}_{s,A}) \leq \#(\mathcal{R}_{1,A})$  leads, summing up to  
 2 all the seeds and dividing by  $M$ , to the upper bound

$$3 \quad \langle n_{3D}(s) \rangle \leq \frac{1}{M} \cdot \sum_A \#(\mathcal{R}_{1,A}) \quad (12)$$

4 thus,  $\langle n_{3D}(s) \rangle$  is necessarily a bounded function. This expression indicates that the  
 5 number of new neighbors when increasing  $s$  exhausts since the number of cells is a  
 6 resource shared by all the layers. It is possible to obtain an upper bound to  
 7  $N_{max} = \lim_{s \rightarrow \infty} \langle n_{3D}(s) \rangle$  since, after a flip in the Delaunay triangulation, the edge  
 8 disappearing (i.e., a cell contact loss) can never be recovered in a cylindrical  
 9 geometry. Thus,  $M \cdot (N_{max} - n_{3D}(1))$  is bounded by the number of edges that  
 10 complement the original Delaunay triangulation on the apical surface, that is,

$$11 \quad N_{max} - \langle n_{3D}(1) \rangle \leq \frac{1}{M} \cdot \left( \frac{M(M-1)}{2} - M \frac{\langle n_{3D}(1) \rangle}{2} \right) = \frac{M-1}{2} - \frac{\langle n_{3D}(1) \rangle}{2} \quad (13)$$

12 leading to

$$13 \quad N_{max} \leq \frac{M-1}{2} + \frac{\langle n_{3D}(1) \rangle}{2} \leq \frac{M-1}{2} + 3 = \frac{M+5}{2} \quad (14)$$

14 Where we have assumed that  $\langle n_{3D}(1) \rangle = 6$ . The simulations of the computational  
 15 Voronoi model and the data of the salivary gland show that  $N_{max}$  is in fact much  
 16 smaller than the theoretical bound  $\frac{M+5}{2}$ .

17

### 18 **A Kolmogorov rate equation for the 3D cellular connectivity**

19 The equation for how the probability,  $P_m$ , of having  $m$  accumulated 3D neighbors  
 20 (i.e.,  $m = n_{3D}$ ) changes as the surface ratio (apico-basal dimensionless radial  
 21 coordinate) increases from  $s$  to  $s + ds$  can be described by the following Markov  
 22 equation (**Fig. 4A-B**),

$$23 \quad P_m(s + ds) = P_m(s)T_{m,m} + P_{m-1}(s)T_{m-1,m} \quad (15)$$

24 where  $T_{n,m}$  is the probability of changing the number of neighbors from  $n$  to  $m$  due  
 25 to an apico-basal intercalation. Since  $\sum_m T_{n,m} = 1$  (normalization of the transition  
 26 probabilities) and  $T_{n,m} = f(n, m) \{ \delta_{n-1,m} + \delta_{n,m+1} \}$  (each intercalation can only  
 27 possibly induce to win one neighbor) then  $T_{m,m} = 1 - T_{m,m+1}$  and the above Markov  
 28 equation can be written as a Kolmogorov equation (a.k.a. Master equation):

$$1 \quad \frac{dP_m(s)}{ds} = P_{m-1}(s)r_{m-1,m} - P_m(s)r_{m,m+1} \quad (16)$$

2 where  $r_{n,m}$  accounts for the probability of apico-basal intercalations per unit of  
 3 surface ratio, i.e.,  $T_{n,m} = r_{n,m} ds$ . We point out that our model accounts for apico-  
 4 basal intercalations that occur due to curvature effects such that  $s = R/R_a$  changes  
 5 along the apico-basal coordinate of cells (i.e., bending, folding). Thus, our model does  
 6 not capture the apico-basal intercalations that develop due to active cellular  
 7 processes (e.g. cellular extrusion, cell divisions) either in bended tissues or in the case  
 8 of tissue planar geometries.

9 By following the Eyring model (Eyring, 1935), i.e., if we assume an Arrhenius-like  
 10 kinetics such that to win neighbors there is an energy cost (see (Bi et al., 2014)) then  
 11  $r_{m,m+1} = \hat{\alpha} e^{-\Delta E_m}$ , where  $\hat{\alpha}$  is the so-called pre-exponential factor that modulates  
 12 the “bare” frequency of intercalations (per unit of surface ratio expansion,  $s$ ) and  
 13  $\Delta E_m$  is a dimensionless activation energy (in units of the effective thermal energy  
 14 associated with membrane fluctuations  $\xi$  (Marmottant et al., 2009)). The observed  
 15 “poor get richer” behavior suggests that the activation energy,  $\Delta E_m$ , increases with  
 16  $m$ . This can be explained as a result of a cumulative process if we assume that each  
 17 neighbor that is gained implies to overcome an energy barrier,  $\beta(s)$ , through an  
 18 apico-basal intercalation. Consequently,  $e^{-\Delta E_m} = \prod_{n=1}^{n=m} e^{-\beta(s)} = e^{-m \cdot \beta(s)}$ . Thus,  
 19  $\beta(s)$  represents the dimensionless activation energy of a cell per 3D neighbor or, in  
 20 the context of the different energetic contributions reviewed in this manuscript, to  
 21 the energy barrier required to perform a spatial T1-transition following a surface  
 22 energy minimization process (Gómez-Gálvez et al., 2018; Mughal et al., 2018). As for  
 23 the dependence of  $\beta$  on  $s$ , the simplest mathematical form that recapitulates the fact  
 24 that the apical and basal surfaces accumulate more cell-cell adherent complexes  
 25 (either in wt or mutant phenotypes) is quadratic (**Fig. S7**):  $\beta(s) = \beta_0 \left(1 + \frac{\delta}{2}(s - s_0)^2\right)$ .  
 26 The average, along the apico-basal coordinate, of the energy cost then  
 27 reads  $\bar{\beta} = 1/(s_b - 1) \int_1^{s_b} \beta(s) ds$ . On the other hand, the mathematical calculations  
 28 indicate that the intercalation rate  $r_{m,m+1}$  becomes null for a finite value of  $m$  or,  
 29 alternatively, that the activation energy becomes infinite for a finite value of  $m$ .  
 30 Otherwise, the net gain of new neighbors is not bounded. This fact can be accounted

1 for by assuming that the bare frequency is a function of the number of neighbors,  
 2  $\hat{\alpha} = \hat{\alpha}(m)$ , such that  $\frac{d\hat{\alpha}}{dm} < 0$  and becomes null for a finite value of  $m$ . For the sake of  
 3 simplicity, we assume that up to first order in  $m$ :  $\hat{\alpha} = \alpha(N_{max} - m)$ , where  $N_{max}$  is  
 4 the asymptotic, maximum, number of 3D neighbors a cell can possibly have.  
 5 Summarizing, the apico-basal intercalation rate  $r_{m,m+1}$  reads,

$$6 \quad r_{m,m+1} = \alpha(N_{max} - m)e^{-m\beta(s)} \quad (17)$$

7 Under these conditions, the Kolmogorov equation reads,

$$8 \quad \frac{dP_m(s)}{ds} = \alpha(N_{max} - (m - 1))e^{-\beta(s)(m-1)}P_{m-1}(s) - \alpha(N_{max} - m)e^{-\beta(s)m}P_m(s)$$

$$9 \quad (18)$$

10 On the other hand, the equation satisfied by the average number of accumulated  
 11 3D neighbors,  $\langle n_{3D} \rangle = \langle m \rangle$ , reads,

$$12 \quad \frac{d\langle m(s) \rangle}{ds} = \sum_m m \frac{dP_m(s)}{ds} = \sum_m r_{m,m+1}P_m(s) = \langle r_{m,m+1} \rangle \quad (19)$$

13 We notice that this equation implies an important role of the disorder (i.e. the  
 14 distribution  $P_m$ ): even in conditions under which the transition rate,  $r_{m,m+1}$ , is  
 15 “large”, the resulting growth of 3D neighbors,  $\frac{d\langle m(s) \rangle}{ds}$ , and, consequently, the net  
 16 accumulation of 3D neighbors, can be more prominent in conditions where the  
 17 transition rate is “small”. To illustrate this effect, we consider the following example.  
 18 For the sake of simplicity, we evaluate the initial growth of 3D neighbors starting  
 19 from the apical surface, i.e. we particularize Eq. (19) to the case  $s = 1$  (and hence  
 20 according to Euler's formula  $\langle P_m(1) \rangle = \sum_m mP_m(1) = 6$ ) and consider two possible  
 21 conditions: a fully ordered ( $o$ ) distribution with  $P_m^o = \delta_{m,6}$  (i.e., all hexagons) and a  
 22 disordered ( $d$ ) condition that combines with equal probability cells with 3, 6, and 9  
 23 sides in the apical surface, i.e.  $P_m^d = \frac{1}{3}(\delta_{m,3} + \delta_{m,6} + \delta_{m,9})$ . We also assume that  
 24  $\beta(s) \simeq \bar{\beta}$  (i.e., we approximate the energy cost to gain new 3D neighbors by its  
 25 average) and that  $\bar{\beta}^o < \bar{\beta}^d$ , and also that  $\alpha^o < \alpha^d$  (**Fig. S9**). Under these conditions,  
 26 for the same  $N_{max}$ , the following holds,  $r_{m,m+1}^o > r_{m,m+1}^d$ , that is, the transition rate  
 27 to gain new 3D neighbors is larger in the ordered case than in the disorder case. This  
 28 is in fact the situation that we observed in the Voronoi tubular model when we

1 estimated the value of the energy barrier to gain new neighbors:  $\alpha$  and  $\beta(s)$   
 2 decrease as the CVT scale increases even though the surface tension energy is  
 3 independent of the CVT scale (see **Fig. S9**, **Fig. 1**, and **Table S1**). However, it is  
 4 possible to find large regions in terms of the values of  $\bar{\beta}^o$ ,  $\bar{\beta}^d$ ,  $\alpha^o$ , and  $\alpha^d$  where  
 5  $\left. \frac{d\langle m(1) \rangle}{ds} \right|_d > \left. \frac{d\langle m(1) \rangle}{ds} \right|_o$  (**Fig. S11**). That is, the growth of 3D neighbors starting from the  
 6 apical surface (i.e.  $s = 1$ ) in the disorder case can be actually larger than that of the  
 7 order case despite the fact that the transition rate to gain new 3D neighbors is  
 8 smaller in the former.

9 Also, from Eq. (19), it is possible to infer, approximately, the expected behavior of  
 10  $\langle m(s) \rangle = \langle n_{3D}(s) \rangle$  as follows. First, by performing a mean-field-like approximation,  
 11 i.e.,  $\langle F(m) \rangle \approx F(\langle m \rangle)$ ,

$$12 \quad \frac{d\langle m \rangle}{ds} \approx \alpha(N_{max} - \langle m \rangle)e^{-\beta(s)\langle m \rangle} \quad (20)$$

13 Second, assuming that  $\beta(s) < 1$  (otherwise it is difficult to justify the observed  
 14 presence of apico-basal intercalations),

$$15 \quad \frac{d\langle m \rangle}{ds} \approx \alpha(N_{max} - \langle m \rangle)(1 - \beta(s)\langle m \rangle) + \mathcal{O}(\beta^2) \quad (21)$$

16 Eq. (21) is formally a logistic-like growth equation that can be solved subjected to the  
 17 condition  $\langle m(1) \rangle = 6$  (the average number of neighbors in the apical surface is 6).

18 We notice that in this case, the disorder levels of the wt and the mutant glands are  
 19 similar. Consequently, the accumulation of 3D neighbors only depends on the  
 20 transition rates,  $r_{m,m+1}$ , that in turn are larger in the mutant background since the  
 21 energy barrier decreases.

22 For finding the parameters of the Kolmogorov model, Eq. (19), that better fit *in silico*  
 23 tubes and salivary glands we implemented an algorithm that solves, numerically, the  
 24 set of equations defined by Eq. (19) and the normalization condition  $\sum_{m=1}^{\infty} P_m(s) = 1$   
 25 to obtain  $\langle m(s) \rangle = \sum_m m P_m(s)$ . Such algorithm minimizes the error between the  
 26 curves  $\langle m(s) \rangle$  obtained in the model and in experiments.

27 The values of the parameters obtained were further used to compare the predicted  
 28 probability distribution of having  $m$  accumulated 3D neighbors for a given value of  $s$ :  
 29  $\{P_m(s)\}$ . We evaluated the relative error of this prediction with respect to the actual

1 distribution from data,  $P_m^{actual}(s)$ , by computing  $\varepsilon^2 = \frac{1}{2} \sum_m \left( P_m^{actual}(s) - P_m(s) \right)^2$ .  
2 This quantity is normalized such that in case of the following situation of full  
3 disagreement between the distributions,  $P_m^{actual}(s) = \delta_{m,i}$  and  $P_m(s) = \delta_{m,j}$  with  
4  $i \neq j$ , provides  $\varepsilon^2 = 1$  (i.e., 100% error).

5

## 6 **Quantitative characterization of spreading in neighbor exchange distributions** 7 **between apical and basal surfaces**

8 In order to characterize the spreading away from the diagonal in the neighbor  
9 exchange distributions between apical and basal surfaces, e.g., **Fig. 2A**, we followed  
10 the same approach used to quantify intrinsic noise during gene expression processes,  
11 see (Elowitz, 2002). Thus,  $\eta^2 = \frac{\langle (n_a - n_b)^2 \rangle}{2\langle n_a \rangle \langle n_b \rangle}$  where  
12  $\langle z(n_a, n_b) \rangle = \sum_{n_a, n_b} z(n_a, n_b) p(n_a, n_b)$ ;  $z$  representing any function of  $n_a$  and  $n_b$   
13 and  $p(n_a, n_b)$  being the probability of neighbor exchange events. We point out that  
14 bins in the diagonal do not correspond necessarily to prismatic cells since a fraction  
15 of cells can conserve the polygonal class in apical and basal surfaces and yet  
16 undergo apico-basal intercalations.

17

## 18 **Statistical comparisons**

19 The characteristics extracted from wildtype and mutant glands were compared by  
20 using a univariate statistical protocol (**Table S1**). This procedure allows to study if the  
21 data from two different groups of data follow a similar distribution: 1) we evaluated  
22 whether features values of these two kinds of glands presented normal distribution  
23 and similar variance using the Shapiro-wilk test and two-sample F-test respectively.  
24 2) If data followed a normal distribution and had similar variance, we employed the  
25 two-tailed Student's t-test. 3) In case, data presented a normal distribution but not  
26 equal variance we employed the two-tailed Welch test to compare means from both  
27 groups. 4) When data did not present normal distribution, we used the Wilcoxon test  
28 to compare medians from both groups.

29 In a different statistical analysis, we tested polygon distribution similarity from  
30 apical and basal surfaces of wildtype and mutant glands and V8 at  $s_a = 1$ ,  $s_b = 1.75$

1 and  $s_b = 10$  (**Table S1**). Following the guidelines from (Sánchez-Gutiérrez et al.,  
2 2016), we implemented chi-squared tests across all samples, being corrected for  
3 multiple testing using the method of Benjamini and Hochberg. To develop a more  
4 robust analysis, we used the distribution of 5-, 6- and 7-sided polygons due to the  
5 low presence (or inexistence) of the other kind of polygons (3-, 4-, 8-, 9-sided cells).

6

#### 7 **Data and code availability**

8 All the necessary materials to reproduce this study are available at Mendeley Data  
9 repository: DOI: 10.17632/gpz68wzhc2.1 and <https://osf.io/nd5t6/>.

1 **REFERENCES**

- 2 **Aldaz, S., Escudero, L. M. and Freeman, M.** (2013). Dual role of myosin II during  
3 *Drosophila* imaginal disc metamorphosis. *Nat. Commun.* **4**, 1761.
- 4 **Alt, S., Ganguly, P. and Salbreux, G.** (2017). Vertex models: from cell mechanics  
5 to tissue morphogenesis. *Philos. Trans. R. Soc. B Biol. Sci.* **372**, 20150520.
- 6 **Ambrosini, A., Gracia, M., Proag, A., Rayer, M., Monier, B. and Suzanne, M.**  
7 (2017). Apoptotic forces in tissue morphogenesis. *Mech. Dev.* **144**, 33–42.
- 8 **Arganda-Carreras, I., Kaynig, V., Rueden, C., Eliceiri, K. W., Schindelin, J.,**  
9 **Cardona, A. and Seung, H. S.** (2017). Trainable Weka Segmentation: A machine  
10 learning tool for microscopy pixel classification. *Bioinformatics* **33**, 2424–2426.
- 11 **Bertet, C., Sulak, L. and Lecuit, T.** (2004). Myosin-dependent junction  
12 remodelling controls planar cell intercalation and axis elongation. *Nature* **429**, 667–  
13 671.
- 14 **Bi, D., Lopez, J. H., Schwarz, J. M. and Manning, M. L.** (2014). Energy barriers  
15 and cell migration in densely packed tissues. *Soft Matter* **10**, 1885.
- 16 **Bi, D., Lopez, J. H., Schwarz, J. M. and Manning, M. L.** (2015). A density-  
17 independent rigidity transition in biological tissues. *Nat. Phys.* **11**, 1074–1079.
- 18 **Blankenship, J. T., Backovic, S. T., Sanny, J. S. P., Weitz, O. and Zallen, J. A.**  
19 (2006). Multicellular Rosette Formation Links Planar Cell Polarity to Tissue  
20 Morphogenesis. *Dev. Cell* **11**, 459–470.
- 21 **Brand, A. H. and Perrimon, N.** (1993). Targeted gene expression as a means of  
22 altering cell fates and generating dominant phenotypes. *Development* **118**, 401–  
23 415.
- 24 **Campàs, O., Mammoto, T., Hasso, S., Sperling, R. A., O’Connell, D., Bischof, A.**  
25 **G., Maas, R., Weitz, D. A., Mahadevan, L. and Ingber, D. E.** (2014). Quantifying cell-  
26 generated mechanical forces within living embryonic tissues. *Nat. Methods* **11**, 183–  
27 189.
- 28 **Canela-Xandri, O., Sagués, F., Casademunt, J. and Buceta, J.** (2011). Dynamics  
29 and mechanical stability of the developing dorsoventral organizer of the wing  
30 imaginal disc. *PLoS Comput. Biol.* **7**,.

- 1        **Cao, J., Guan, G., Ho, V. W. S., Wong, M.-K., Chan, L.-Y., Tang, C., Zhao, Z. and**  
2 **Yan, H.** (2020). Establishment of a morphological atlas of the *Caenorhabditis*  
3 *elegans* embryo using deep-learning-based 4D segmentation. *Nat. Commun.* **11**,  
4 6254.
- 5        **Clevers, H.** (2016). Modeling Development and Disease with Organoids. *Cell* **165**,  
6 1586–1597.
- 7        **Colas, J.-F. and Schoenwolf, G. C.** (2001). Towards a cellular and molecular  
8 understanding of neurulation. *Dev. Dyn.* **221**, 117–145.
- 9        **Curran, S., Strandkvist, C., Bathmann, J., de Gennes, M., Kabla, A., Salbreux, G.**  
10 **and Baum, B.** (2017). Myosin II Controls Junction Fluctuations to Guide Epithelial  
11 Tissue Ordering. *Dev. Cell* **43**, 480-492.e6.
- 12        **Elowitz, M. B.** (2002). Stochastic Gene Expression in a Single Cell. *Science* (80-. ).  
13 **297**, 1183–1186.
- 14        **Euler, L.** (1767). *Solutio facilis problematum quorundam geometricorum*  
15 *difficillimorum*. Novi Commentarii academiae scientiarum Petropolitanae.
- 16        **Eyring, H.** (1935). The activated complex in chemical reactions. *J. Chem. Phys.* **3**,  
17 63–71.
- 18        **Farhadifar, R., Röper, J.-C., Aigouy, B., Eaton, S. and Jülicher, F.** (2007). The  
19 Influence of Cell Mechanics, Cell-Cell Interactions, and Proliferation on Epithelial  
20 Packing. *Curr. Biol.* **17**, 2095–2104.
- 21        **Fletcher, A. G., Osterfield, M., Baker, R. E. and Shvartsman, S. Y.** (2014). Vertex  
22 Models of Epithelial Morphogenesis. *Biophys. J.* **106**, 2291–2304.
- 23        **Founounou, N., Farhadifar, R., Collu, G. M., Weber, U., Shelley, M. J. and**  
24 **Mlodzik, M.** (2021). Tissue fluidity mediated by adherens junction dynamics  
25 promotes planar cell polarity-driven ommatidial rotation. *Nat. Commun.* **12**, 6974.
- 26        **Franco-Barranco, D., Muñoz-Barrutia, A. and Arganda-Carreras, I.** (2021). Stable  
27 Deep Neural Network Architectures for Mitochondria Segmentation on Electron  
28 Microscopy Volumes. *Neuroinformatics* **1**, 1–14.
- 29        **Gelbart, M. A., He, B., Martin, A. C., Thiberge, S. Y., Wieschaus, E. F. and**  
30 **Kaschube, M.** (2012). Volume conservation principle involved in cell lengthening

- 1 and nucleus movement during tissue morphogenesis. *Proc. Natl. Acad. Sci.* **109**,  
2 19298–19303.
- 3 **Gibson, M. C., Patel, A. B., Nagpal, R. and Perrimon, N.** (2006). The emergence  
4 of geometric order in proliferating metazoan epithelia. *Nature* **442**, 1038–1041.
- 5 **Gibson, W. T., Veldhuis, J. H., Rubinstein, B., Cartwright, H. N., Perrimon, N.,**  
6 **Brodland, G. W., Nagpal, R. and Gibson, M. C.** (2011). Control of the mitotic  
7 cleavage plane by local epithelial topology. *Cell* **144**, 427–438.
- 8 **Gilbert, S. F. and Barresi, M. J. F.** (2013). *Developmental Biology. 10th ed.*  
9 Sinauer Associates.
- 10 **Girdler, G. C. and Roper, K.** (2014). Controlling cell shape changes during salivary  
11 gland tube formation in *Drosophila*. *Semin Cell Dev Biol* **31**, 74–81.
- 12 **Gómez-Gálvez, P., Vicente-Munuera, P., Tagua, A., Forja, C., Castro, A. M. A.**  
13 **M., Letrán, M., Valencia-Expósito, A., Grima, C., Bermúdez-Gallardo, M., Serrano-**  
14 **Pérez-Higueras, Ó., et al.** (2018). Scutoids are a geometrical solution to three-  
15 dimensional packing of epithelia. *Nat. Commun.* **9**, 2960.
- 16 **Gómez-Gálvez, P., Vicente-Munuera, P., Anbari, S., Buceta, J. and Escudero, L.**  
17 **M.** (2021a). The complex three-dimensional organization of epithelial tissues.  
18 *Development* **148**, dev195669.
- 19 **Gómez-Gálvez, P., Anbari, S., Escudero, L. M. and Buceta, J.** (2021b). Mechanics  
20 and self-organization in tissue development. *Semin. Cell Dev. Biol.* **120**, 147–159.
- 21 **Gómez, H. F., Dumond, M. S., Hodel, L., Vetter, R. and Iber, D.** (2021). 3D cell  
22 neighbour dynamics in growing pseudostratified epithelia. *Elife* **10**,.
- 23 **Guignard, L., Fiúza, U.-M., Leggio, B., Laussu, J., Faure, E., Michelin, G., Biasuz,**  
24 **K., Hufnagel, L., Malandain, G., Godin, C., et al.** (2020). Contact area-dependent  
25 cell communication and the morphological invariance of ascidian embryogenesis.  
26 *Science (80-. ).* **369**, eaar5663.
- 27 **Hammond, S. M., Bernstein, E., Beach, D. and Hannon, G. J.** (2000). An RNA-  
28 directed nuclease mediates post-transcriptional gene silencing in *Drosophila* cells.  
29 *Nature* **404**, 293–296.
- 30 **Hirashima, T. and Adachi, T.** (2019). Polarized cellular mechano-response system

- 1 for maintaining radial size in developing epithelial tubes. *Development* **146**,  
2 dev181206.
- 3 **Honda, H.** (1978). Description of cellular patterns by Dirichlet domains: The two-  
4 dimensional case. *J. Theor. Biol.* **72**, 523–543.
- 5 **Huch, M., Knoblich, J. A., Lutolf, M. P. and Martinez-Arias, A.** (2017). The hope  
6 and the hype of organoid research. *Development* **144**, 938–941.
- 7 **Huebner, R. J. and Ewald, A. J.** (2014). Cellular foundations of mammary  
8 tubulogenesis. *Semin. Cell Dev. Biol.* **31**, 124–131.
- 9 **Inoue, Y., Tateo, I. and Adachi, T.** (2019). Epithelial tissue folding pattern in  
10 confined geometry. *Biomech. Model. Mechanobiol.*
- 11 **Ioannou, F., Dawi, M. A., Tetley, R. J., Mao, Y. and Muñoz, J. J.** (2020).  
12 Development of a New 3D Hybrid Model for Epithelia Morphogenesis. *Front.*  
13 *Bioeng. Biotechnol.* **8**,.
- 14 **Iruela-Arispe, M. L. and Beitel, G. J.** (2013). Tubulogenesis. *Development*.
- 15 **Irvine, K. D. and Wieschaus, E.** (1994). Cell intercalation during *Drosophila*  
16 germband extension and its regulation by pair-rule segmentation genes.  
17 *Development* **120**, 827–841.
- 18 **Latorre, E., Kale, S., Casares, L., Gómez-González, M., Uroz, M., Valon, L., Nair,**  
19 **R. V., Garreta, E., Montserrat, N., del Campo, A., et al.** (2018). Active  
20 superelasticity in three-dimensional epithelia of controlled shape. *Nature* **563**, 203–  
21 208.
- 22 **Leptin, M. and Grunewald, B.** (1990). Cell shape changes during gastrulation in  
23 *Drosophila*. *Development* **110**, 73–84.
- 24 **Lewis, F. T.** (1928). The correlation between cell division and the shapes and  
25 sizes of prismatic cells in the epidermis of cucumis. *Anatom. Rec.* **38**, 341–376.
- 26 **Lloyd, S.** (1982). Least squares quantization in PCM. *IEEE Trans. Inf. Theory* **28**,  
27 129–137.
- 28 **Machado, S., Mercier, V. and Chiaruttini, N.** (2019). LimeSeg: a coarse-grained  
29 lipid membrane simulation for 3D image segmentation. *BMC Bioinformatics* **20**, 2.
- 30 **Mao, Y., Tournier, A. L., Hoppe, A., Kester, L., Thompson, B. J. and Tapon, N.**

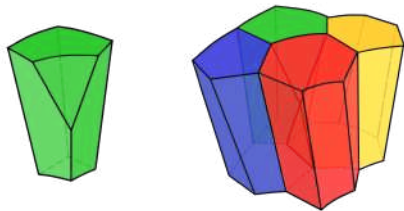
- 1 (2013). Differential proliferation rates generate patterns of mechanical tension that  
2 orient tissue growth. *EMBO J.* **32**, 2790–2803.
- 3 **Marmottant, P., Mgharbel, A., Käfer, J., Audren, B., Rieu, J. P., Vial, J. C., Van**  
4 **Der Sanden, B., Marée, A. F. M., Graner, F. and Delanoë-Ayari, H.** (2009). The role  
5 of fluctuations and stress on the effective viscosity of cell aggregates. *Proc. Natl.*  
6 *Acad. Sci. U. S. A.* **106**, 17271–17275.
- 7 **Messal, H. A., Alt, S., Ferreira, R. M. M., Gribben, C., Wang, V. M.-Y., Cotoi, C.**  
8 **G., Salbreux, G. and Behrens, A.** (2019). Tissue curvature and apicobasal  
9 mechanical tension imbalance instruct cancer morphogenesis. *Nature* **566**, 126.
- 10 **Misra, M., Audoly, B. and Shvartsman, S. Y.** (2017). Complex structures from  
11 patterned cell sheets. *Philos. Trans. R. Soc. B Biol. Sci.* **372**, 20150515.
- 12 **Mongera, A., Rowghanian, P., Gustafson, H. J., Shelton, E., Kealhofer, D. A.,**  
13 **Carn, E. K., Serwane, F., Lucio, A. A., Giammona, J. and Campàs, O.** (2018). A fluid-  
14 to-solid jamming transition underlies vertebrate body axis elongation. *Nature* **561**,  
15 401–405.
- 16 **Mughal, A., Cox, S. J., Weaire, D., Burke, S. R. and Hutzler, S.** (2018).  
17 Demonstration and interpretation of ‘scutoid’ cells formed in a quasi-2D soap froth.  
18 *Philos. Mag. Lett.* **98**, 358–364.
- 19 **Nelson, C. M.** (2009). Geometric control of tissue morphogenesis. *Biochim.*  
20 *Biophys. Acta - Mol. Cell Res.* **1793**, 903–910.
- 21 **Nelson, C. M., Jean, R. P., Tan, J. L., Liu, W. F., Sniadecki, N. J., Spector, A. A.**  
22 **and Chen, C. S.** (2005). Emergent patterns of growth controlled by multicellular  
23 form and mechanics. *Proc. Natl. Acad. Sci.*
- 24 **Odell, G. M., Oster, G., Alberch, P. and Burnside, B.** (1981). The mechanical basis  
25 of morphogenesis. I. Epithelial folding and invagination. *Dev. Biol.* **85**, 446–462.
- 26 **Okuda, S., Kuranaga, E. and Sato, K.** (2019). Apical Junctional Fluctuations Lead  
27 to Cell Flow while Maintaining Epithelial Integrity. *Biophys. J.* **116**, 1159–1170.
- 28 **Pérez-González, C., Alert, R., Blanch-Mercader, C., Gómez-González, M.,**  
29 **Kolodziej, T., Bazellieres, E., Casademunt, J. and Trepap, X.** (2019). Active wetting  
30 of epithelial tissues. *Nat. Phys.* **15**, 79–88.

- 1        **Petridou, N. I., Corominas-Murtra, B., Heisenberg, C.-P. and Hannezo, E.** (2021).  
2 Rigidity percolation uncovers a structural basis for embryonic tissue phase  
3 transitions. *Cell* **184**, 1914–1928.e19.
- 4        **Pilot, F. and Lecuit, T.** (2005). Compartmentalized morphogenesis in epithelia:  
5 from cell to tissue shape. *Dev Dyn* **232**, 685–694.
- 6        **Reinhardt, K.** (1918). Über die Zerlegung der Ebene in Polygone.  
7        **Röper, K.** (2018). Quantitative Imaging and the Effect of Tissue Topology on  
8 Morphogenesis. *Dev. Cell* **47**, 537–538.
- 9        **Rupprecht, J. F., Ong, K. H., Yin, J., Huang, A., Dinh, H. H. Q., Singh, A. P., Zhang,**  
10 **S., Yu, W. and Saunders, T. E.** (2017). Geometric constraints alter cell arrangements  
11 within curved epithelial tissues. *Mol. Biol. Cell* **28**, 3582–3594.
- 12        **Sanchez-Corrales, Y. E., Blanchard, G. B. and Röper, K.** (2018). Radially  
13 patterned cell behaviours during tube budding from an epithelium. *Elife* **7**, .
- 14        **Sanchez-Gutierrez, D., Tozluoglu, M., Barry, J. D., Pascual, A., Mao, Y. and**  
15 **Escudero, L. M.** (2016). Fundamental physical cellular constraints drive self-  
16 organization of tissues. *EMBO J* **35**, 77–88.
- 17        **Sánchez-Gutiérrez, D., Tozluoglu, M., Barry, J. D., Pascual, A., Mao, Y. and**  
18 **Escudero, L. M.** (2016). Fundamental physical cellular constraints drive  
19 self-organization of tissues. *EMBO J.* **35**, 77–88.
- 20        **Schindelin, J., Arganda-Carreras, I., Frise, E., Kaynig, V., Longair, M., Pietzsch, T.,**  
21 **Preibisch, S., Rueden, C., Saalfeld, S., Schmid, B., et al.** (2012). Fiji: an open-source  
22 platform for biological-image analysis. *Nat. Methods* **9**, 676–682.
- 23        **Schutgens, F., Rookmaaker, M. B., Margaritis, T., Rios, A., Ammerlaan, C.,**  
24 **Jansen, J., Gijzen, L., Vormann, M., Vonk, A., Viveen, M., et al.** (2019). Tubuloids  
25 derived from human adult kidney and urine for personalized disease modeling. *Nat.*  
26 *Biotechnol.* **37**, 303–313.
- 27        **Shahbazi, M. N., Siggia, E. D. and Zernicka-Goetz, M.** (2019). Self-organization of  
28 stem cells into embryos: A window on early mammalian development. *Science* (80-  
29 ). **364**, 948–951.
- 30        **Sharma, P., Saraswathy, V. M., Xiang, L. and Furthauer, M.** (2019). Delta/Notch

- 1 signaling controls neuroepithelial morphogenesis in the zebrafish spinal cord.  
2 *bioRxiv* 517714.
- 3 **Siedlik, M. J., Manivannan, S., Kevrekidis, I. G. and Nelson, C. M.** (2017). Cell  
4 Division Induces and Switches Coherent Angular Motion within Bounded Cellular  
5 Collectives. *Biophys. J.* **112**, 2419–2427.
- 6 **Spencer, M. A., Jabeen, Z. and Lubensky, D. K.** (2017). Vertex stability and  
7 topological transitions in vertex models of foams and epithelia. *Eur. Phys. J. E* **40**, 2.
- 8 **Sugimura, K., Lenne, P.-F. F. and Graner, F.** (2016). Measuring forces and  
9 stresses in situ in living tissues. *Development* **143**, 186–196.
- 10 **Swanson, L. E. and Beitel, G. J.** (2006). Tubulogenesis: an inside job. *Curr Biol* **16**,  
11 R51-3.
- 12 **Tepass, U., Gruszynski-DeFeo, E., Haag, T. A., Omatyar, L., Török, T. and**  
13 **Hartenstein, V.** (1996). shotgun encodes *Drosophila* E-cadherin and is preferentially  
14 required during cell rearrangement in the neurectoderm and other  
15 morphogenetically active epithelia. *Genes Dev.* **10**, 672–685.
- 16 **Thompson, D. W. D.** (1945). *On growth and form*. Cambridge university press.
- 17 **Trepat, X., Wasserman, M. R., Angelini, T. E., Millet, E., Weitz, D. A., Butler, J. P.**  
18 **and Fredberg, J. J.** (2009). Physical forces during collective cell migration. *Nat. Phys.*  
19 **5**, 426–430.
- 20 **Tung, J. J., Tattersall, I. W. and Kitajewski, J.** (2012). Tips, Stalks, Tubes: Notch-  
21 Mediated Cell Fate Determination and Mechanisms of Tubulogenesis during  
22 Angiogenesis. *Cold Spring Harb. Perspect. Med.* **2**, a006601–a006601.
- 23 **Vicente-Munuera, P., Gómez-Gálvez, P., Tetley, R. J., Forja, C., Tagua, A.,**  
24 **Letrán, M., Tozluoglu, M., Mao, Y. and Escudero, L. M.** (2020). EpiGraph: an open-  
25 source platform to quantify epithelial organization. *Bioinformatics* **36**, 1314–1316.
- 26 **Wetzel, G.** (1926). Zur entwicklungsmechanischen Analyse des einfachen  
27 prismatischen Epithels. *Wilhelm Roux Arch. für Entwicklungsmechanik der Org.*
- 28 **Wolny, A., Cerrone, L., Vijayan, A., Tofanelli, R., Barro, A. V., Louveaux, M.,**  
29 **Wenzl, C., Strauss, S., Wilson-Sánchez, D., Lymbouridou, R., et al.** (2020). Accurate  
30 and versatile 3D segmentation of plant tissues at cellular resolution. *Elife* **9**,.

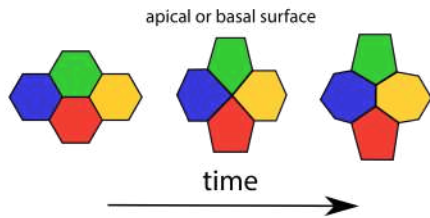
- 1        **Yang, X., Bi, D., Czajkowski, M., Merkel, M., Manning, M. L. and Marchetti, M.**  
2        **C.** (2017). Correlating cell shape and cellular stress in motile confluent tissues. *Proc.*  
3        *Natl. Acad. Sci.* **114**, 12663–12668.
- 4        **Yang, R., Li, E., Kwon, Y. J., Mani, M. and Beitel, G. J.** (2019). QuBiT: a  
5        quantitative tool for analyzing epithelial tubes reveals unexpected patterns of  
6        organization in the *Drosophila* trachea. *Development* **146**,.
- 7        **Zallen, J. A. and Zallen, R.** (2004). Cell-pattern disordering during convergent  
8        extension in *Drosophila*. *J. Phys. Condens. Matter* **16**, S5073–S5080.
- 9  
10  
11

A



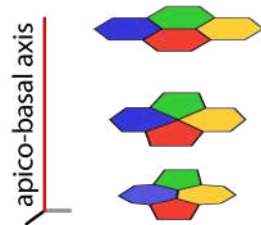
Scutoids

B



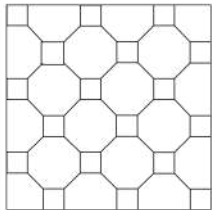
T1-transition

C



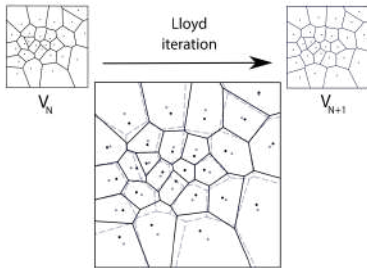
Apico-basal transition

D



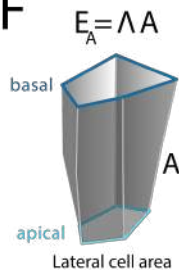
Tessellation

E



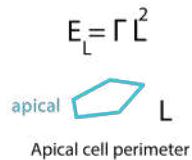
Voronoi diagram

F



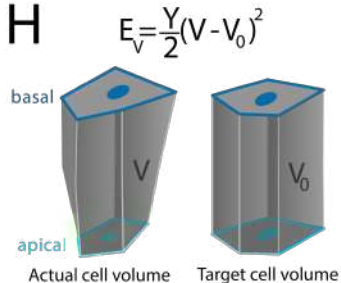
Surface tension energy

G

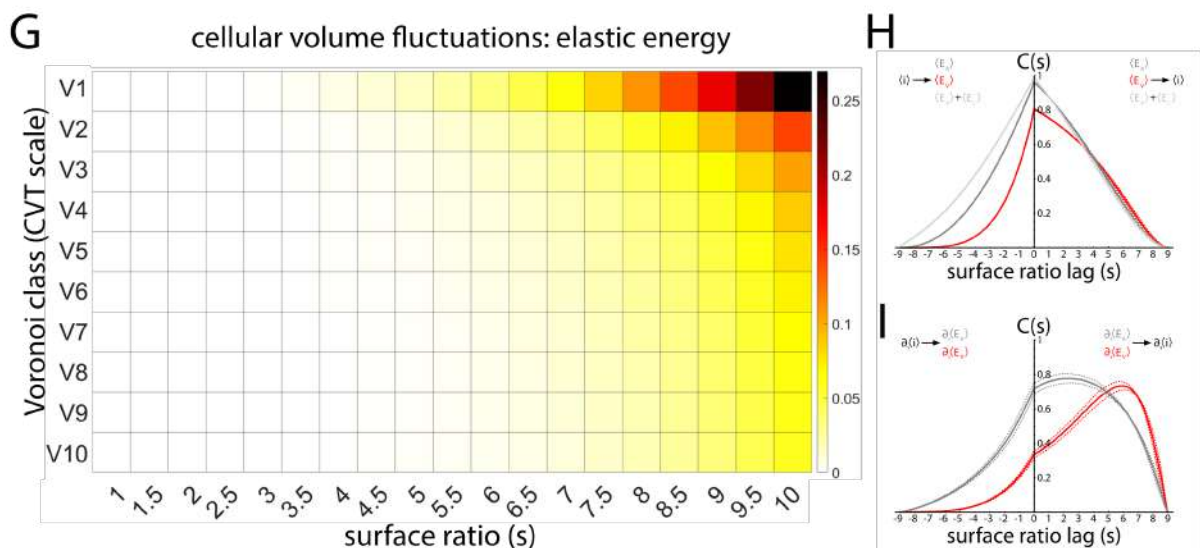
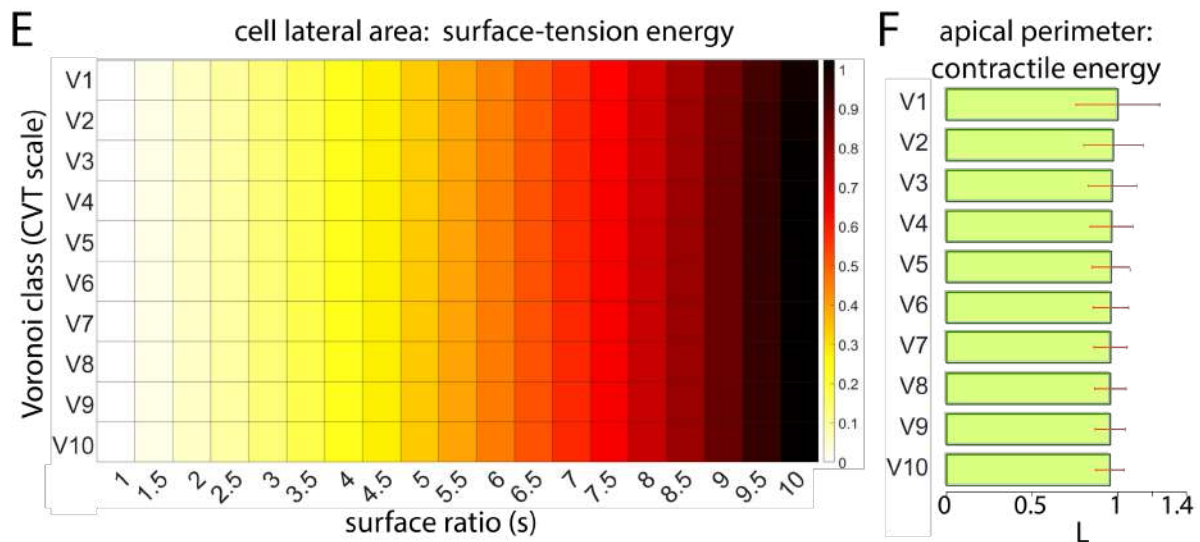
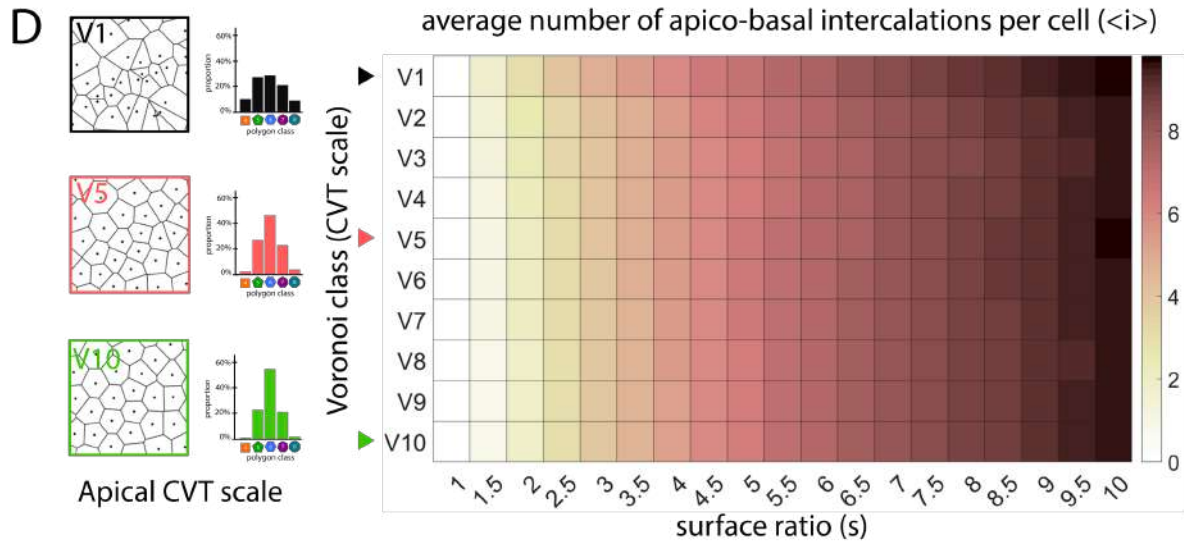
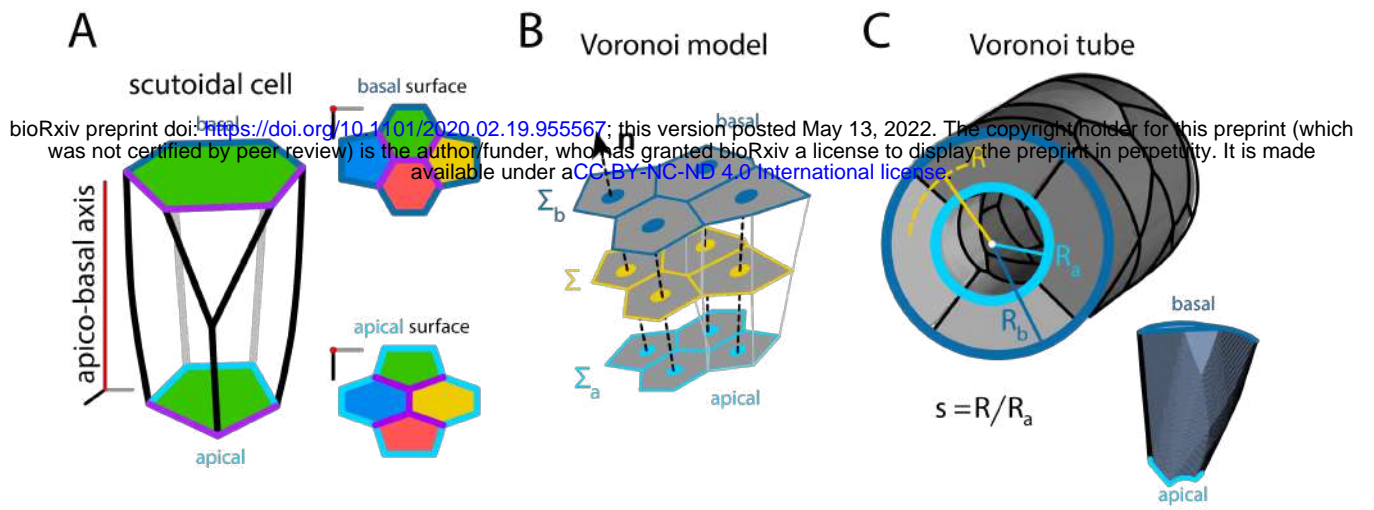


Contractile energy

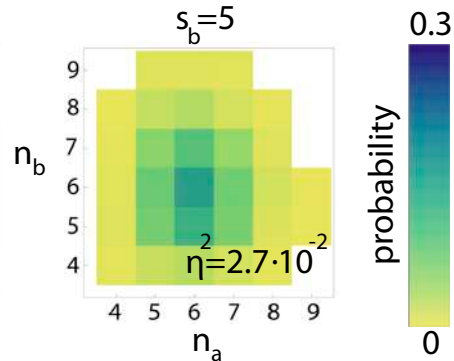
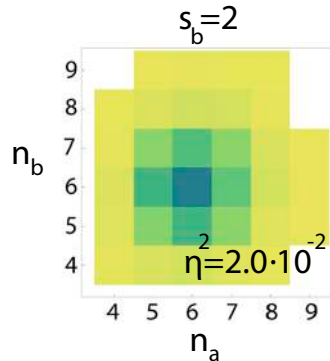
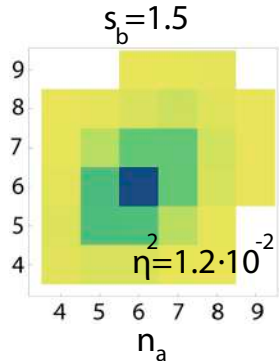
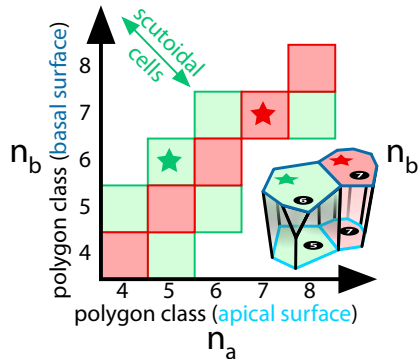
H



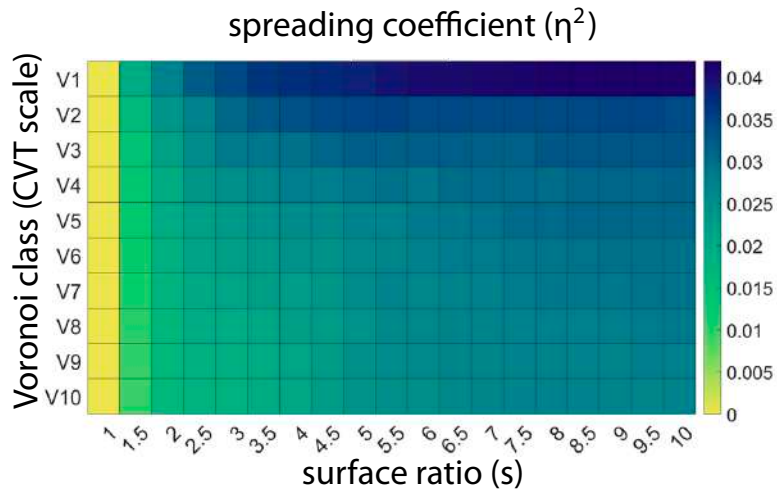
Elastic energy



A



B



C

